Journal of Controlled Release 367 (2024) 300–315

Contents lists available at ScienceDirect

Journal of Controlled Release

journal homepage: www.elsevier.com/locate/jconrel

Biomimetic bright optotheranostics for metastasis monitoring and multimodal image-guided breast cancer therapeutics

Rajendra Prasad [a,b,**], Berney Peng [g], Bárbara B. Mendes [f,1], Hailey I. Kilian [c,1], Mahadeo Gorain [d,1], Huijuan Zhang [c,1], Gopal Chandra Kundu [d,e], Jun Xia [c], Jonathan F. Lovell [c], João Conde [f,*]

[a] School of Biochemical Engineering, Indian Institute of Technology (BHU), Varanasi 221005, India
[b] Department of Mechanical Engineering, Tufts University, Medford, MA 02155, USA
[c] Department of Biomedical Engineering, University at Buffalo, State University of New York, Buffalo 14260, NY, USA
[d] Laboratory of Tumor Biology, Angiogenesis and Nanomedicine Research, National Center for Cell Science, Pune 411007, India
[e] School of Biotechnology and Kalinga Institute of Medical Sciences (KIMS), KIIT Deemed to be University, Bhubaneswar 751024, India
[f] ToxOmics, NOVA Medical School, Faculdade de Ciências Médicas, NMS|FCM, Universidade NOVA de Lisboa, Lisboa, Portugal
[g] Department of Pathology and Laboratory Medicine, David Geffen School of Medicine, University of California at Los Angeles, Los Angeles, CA 90095, United States

ARTICLE INFO

Keywords:
Biomimetic
Bright optotheranostics
Solid tumor
Metastasis
Multimodal imaging and therapy

ABSTRACT

Nanoparticle formulations blending optical imaging contrast agents and therapeutics have been a cornerstone of preclinical theranostic applications. However, nanoparticle-based theranostics clinical translation faces challenges on reproducibility, brightness, photostability, biocompatibility, and selective tumor targeting and penetration. In this study, we integrate multimodal imaging and therapeutics within cancer cell-derived nanovesicles, leading to biomimetic bright optotheranostics for monitoring cancer metastasis. Upon NIR light irradiation, the engineered optotheranostics enables deep visualization and precise localization of metastatic lung, liver, and solid breast tumors along with solid tumor ablation. Metastatic cell-derived nanovesicles (~80 ± 5 nm) are engineered to encapsulate imaging (emissive organic dye and gold nanoparticles) and therapeutic agents (anticancer drug doxorubicin and photothermally active organic indocyanine green dye). Systemic administration of biomimetic bright optotheranostic nanoparticles shows escape from mononuclear phagocytic clearance with (i) rapid tumor accumulation (3 h) and retention (up to 168 h), (ii) real-time monitoring of metastatic lung, liver, and solid breast tumors and (iii) 3-fold image-guided solid tumor reduction. These findings are supported by an improvement of X-ray, fluorescence, and photoacoustic signals while demonstrating a tumor reduction (201 mm^3) in comparison with single therapies that includes chemotherapy (134 mm^3), photodynamic therapy (72 mm^3), and photothermal therapy (88 mm^3). The proposed innovative platform opens new avenues to improve cancer diagnosis and treatment outcomes by allowing the monitorization of cancer metastasis, allowing the precise cancer imaging, and delivering synergistic therapeutic agents at the solid tumor site.

Solid tumor heterogeneity and circulating tumor cells, especially in breast cancer [1–3], often leads to the metastatic spread of cancer cells and ultimately, death. Tumor heterogeneity also leads to a decline in therapeutic response resulting in tumor (i) recurrence, (ii) drug resistance and (iii) metastasis [4,5]. Despite the current treatment options, such as surgery, radiotherapy, chemotherapeutic drugs, and antibodies, there is still a significant cancer-associated mortality and adverse side effects arising from these approaches [6–11]. In solid tumors, imaging contrast agents demonstrated a rapid clearance, poor targeting, nonspecific tissue distribution, a limited tumor visualization [11–15], and thus nanohybrid systems are now developed for solid tumors in preclinical models [14–17]. Recent advances in nanoimaging and therapeutics platforms (metallic and nonmetallic) could solve major obstacles to conventional diagnostics and therapies [15–21]. In the last 20–25

* Corresponding author.
** Corresponding author at: School of Biochemical Engineering, Indian Institute of Technology (BHU), Varanasi 221005, India.
E-mail addresses: rajendra.bce@iitbhu.ac.in, rajendra.prasad@tufts.edu (R. Prasad), joao.conde@nms.unl.pt (J. Conde).
[1] Equal contribution

https://doi.org/10.1016/j.jconrel.2024.01.056
Received 27 October 2023; Received in revised form 15 January 2024; Accepted 25 January 2024
Available online 30 January 2024

years, metallic and nonmetallic nanoparticle (NP)-based imaging and therapeutic systems have been designed and tested in solid tumor models [15,20–22], and various biological and physicochemical parameters of these platforms have been investigated in in vivo applications [23–27]. Among the thousands of proposed nanoparticle systems, only a few (liposomes, silica, gold, iron and polymeric-based systems) have reached in clinical testing [28–34]. More recently, nanoparticles-based theranostics or "imaging integrated therapeutic systems" have been developed for imaging-guided solid tumor ablation [35–37]. However, these nano-based systems need to circumnavigate heterogeneous tumor microenvironments, which still face the major issues related to tumor penetration, tumor entry, tumor retention, site-selective tumor accumulation, specific biodistribution, circulation half-life, and in vivo biosafety and biocompatibility [38–40]. Moreover, brightness and dose dependent efficacy of nanosized platforms are less explored, which are important parameters for deep visualization of solid tumors in the body [41–44]. Apart from these concerns, synthetic nanoparticles require surface modifications with stabilizing agents and targeting ligands to identify selective binding with cancer cells, which hamper their physicochemical properties [37,43]. In addition, several questions remain unanswered: (i) how can nanoparticles be designed to improve tumor uptake and retention following systemic administration to provide better resolution of tumors with site-selectivity, (ii) how many dyes per nanoparticle are required to achieve better brightness from solid tumor area and metastasis monitoring of the solid tumor, and (iii) at what distance (tumor periphery to deep core) will these injected particles distribute or transport in a heterogeneous tumor environment [43–45].

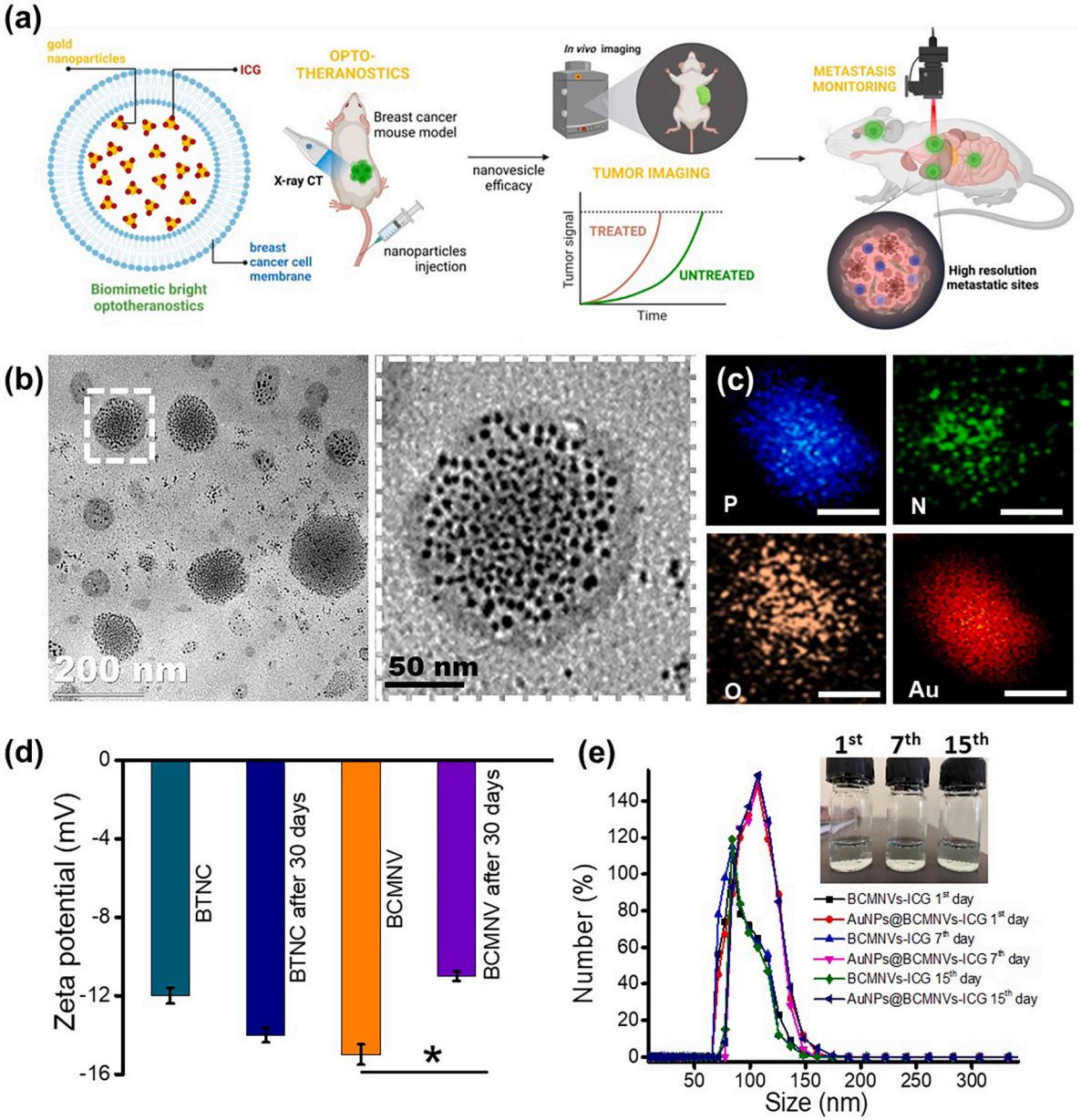

Fig. 1. (a) Schematic representation and characteristics tumor-mimetic bright optotheranostics for metastasis monitoring and multimodal image guided breast cancer therapeutics, (b) TEM images of gold nanoparticles integrated cancer cells derived membrane nanovesicles (AuNPs@BCMVs), (c) elemental mapping analysis of AuNPs@BCMVs, (d) zeta potential surface charge measurements of engineered tumor-mimetic bright optotheranostics (BTNC) and cancer cells derived membrane nanovesicles (BCMNVs) at first and 30th day and (e) dynamic light scattering (DLS) measurements of various designed nanoparticles and inset digital photograph of their aqueous suspensions. $^{*}p < 0.05$. All measurements were performed in triplicate ($n = 3$). (For interpretation of the references to color in this figure legend, the reader is referred to the web version of this article.)

In the last few years, both cancerous and noncancerous cells have been used to produce biomimetic imaging and therapeutic delivery platforms [46,47]. Cell-derived biomimetic nanovesicles have recently been proposed as carriers for delivering either imaging or therapeutic agents to solid tumors. Although they are yet to be used to carry both imaging and therapeutics and perform theranostics response at the targeted site upon external stimuli [47]. These cell-derived nanovesicles platforms face engineering challenges, such as low product yield and poor repeatability, minimal improvement in nonspecific biodistribution, and poor site-selective tumor uptake and retention [46–48]. Most importantly, cancer cells-derived biomimetic systems have been minimally tested for metastasis monitoring of solid tumors. Here, we integrated multiple imaging, namely X-ray computed tomography (X-ray CT), near infra-red fluorescence (NIRF), and photoacoustic imaging (PA), and therapeutics agents that includes chemotherapy (chemo), photodynamic therapy (PDT), and photothermal therapy (PTT) within a single biomimetic nanosystem (Fig.1a). To achieve this, photothermally active emissive organic dyes and plasmonic gold nanoparticles (AuNPs) are integrated within tumor cell-derived nanovesicles (AuNPs@BCMNVs) followed by encapsulation of doxorubicin (DOX). The engineered theranostics system is evaluated for (i) lung and liver metastasis monitoring, (ii) multimodal image guided breast tumor reduction, and (iii) combination therapeutics of solid tumor with selective visualization/brightness. The engineered single nanovesicle platform mimics the surface of tumor cells along with high fluorescent optotheranostics (optically active imaging and therapeutics) ability enables a comprehensive cancer metastasis monitoring, multimodal imaging, and solid tumor reduction upon NIR light irradiation.

1. Engineered biomimetic bright optotheranostics development and characterization

For solid tumor imaging and therapeutics, we have engineered AuNPs@BCMNVs as bright optotheranostics by integrating multimodal imaging (emissive organic dye and AuNPs) and therapeutics (anticancer drug DOX and photothermally ICG dye) probes. These biomimetic fluorescent optotheranostic nanoparticles were engineered from metastatic 4 T1 murine cells by cell lysis, hypotonic treatment, and self-assembly processes. Sonication was used for disrupting the cell membrane to allow the penetration of surface-modified AuNPs (~ 6 nm) to produce engineered AuNPs@BCMNVs. Uniform size (~80 ± 5 nm) and morphology of engineered AuNPs@BCMNVs (40 mg/batch, 1.2×10^{11} particles/cm^3) were examined by cryo-mode microscopic imaging (Fig. 1b). The integration of AuNPs was clearly seen in the core of nanovesicles, which was further corroborated with elemental mapping (Au in red, N in green, P in blue and O in light red color), selected area electron diffraction (SAED) and dark field imaging (Fig. 1c, S1a, b). Further, energy-dispersive X-ray analysis (EDAX) analysis showed the presence of AuNPs within BCMVs (Fig. S2a). Empty BCMNVs obtained from cell lysis, hypotonic treatment, sonication, and self-assembly processes were clearly seen from microscopic imaging (Fig. S2b), showing a negative surface charge (−15 mV), which was maintained for 15 days (Fig. 1d). Once integrated with AuNPs and ICG, BCMNVs demonstrated slightly lower negative surface charge (−14 and − 12 mV) compared to parent BCMNVs. The surface charge data indicated about better colloidal stability of engineered nanoparticles, which means particles were free from aggregation (no turbidity) that was correlated with the aqueous dispersions of engineered NP at 0.1 mg/mL (Fig. S2c). Further, the effect of bovine serum albumin (BSA) on NP diameter was measured by incubating engineered NPs for 6 h at 37 °C. NP diameter measured by dynamic light scattering (DLS) were 100 ± 5 nm in the first week and slightly reduced to 85 ± 5 nm after two weeks. This result can be explained by the degradation of AuNPs@BCMNVs (Fig. 1e, Fig. S3). Little to no turbidity was observed from the aqueous dispersion of NPs at 0.1 mg/mL, indicating their purity and stability after purification by centrifugation (8000 rpm for 20 min) and dialysis (2 days, Fig. S4).

Optical characterization was used to evaluate the photonic properties of AuNPs@BCMNVs after encapsulation of ICG dye (Fig. 2a-e). ICG serves a dual role as both a red emissive imaging agent and photothermally active therapeutic. In photoluminescence measurements, peak broadening and red shifting were observed in AuNPs@BCMNVs-ICG and BCMNVs-ICG conditions compared to free ICG dye (Fig. 2a). Particle size measurements of AuNPs@BCMNVs-ICG and BCMNVs-ICG demonstrated better colloidal stability in aqueous media (Fig. 2b). Regarding photostability, free ICG dye fluorescence decreased after 2 days whereas ICG encapsulated nanovesicles (both AuNPs@BCMNVs and BCMNVs) maintained their emission intensity over 15 days (Fig. S5, S6). In absorption spectroscopy measurements, red shifts (from 780 to 788 nm) were noticed in both BCMNVs-ICG (1.52×10^{-6} M) and AuNPs@BCMNVs-ICG (1.71×10^{-6} M) compared to free ICG dye (779, 2.09×10^{-6} M) (Fig. 2c, d). AuNPs@BCMNVs-ICG NPs also showed an additional peak at 521 nm, indicating the presence of small AuNPs. Broad scattering between 250 and 400 nm was noticed in the UV–Vis-NIR absorption spectra of AuNPs@BCMNVs-ICG compared to free ICG and AuNPs, which indicated the presence of large size NPs (Fig. 2c-e). Aqueous suspension of free AuNPs showed negligible scattering between 250 and 400 nm due to their small size (~6 nm). ICG and AuNP peaks seen in AuNPs@BCMNVs-ICG were not seen in the empty control (BCMNV, Fig. 2d).

Spectroscopic measurements evaluated the relative brightness of engineered biomimetic NPs, which was calculated in MESF units (Molecules of Equivalent Soluble Fluorochrome) that is a standard metric used in flow cytometry (Fig. 2e). The brightness measurements comparisons revealed that an individual AuNPs@BCMNVs-ICG particle excited at 789 nm was equivalent to the fluorescence from 858 molecules of free ICG dye. During blood circulation, AuNPs@BCMNVs-ICG NPs demonstrated better photoemission signal intensity than the other tested conditions with brightness variations from 468 to 886 (Fig. 2e). The increased brightness of AuNPs@BCMNVs-ICG may be due to the interaction between surface markers of nanovesicles and ICG dye. Strikingly, strong interactions between ICG dye with cell membrane biomarkers and proteins have been previously discussed [49]. AuNPs@BCMNVs-ICG were examined by absorbance spectroscopic measurements followed by linearity of AuNPs (R^2 0.98) and ICG (R^2 0.99) at various concentrations (0.1–0.5 mM), as shown in Fig. S7. AuNPs and ICG dye have showed optimal optical properties for (i) NIRF and PA imaging and (ii) NIR light triggered PTT and PDT therapies [50–52]. These nanosized imaging and therapeutics probes have been integrated with synthetic platform for fulfilling theranostics requirements. But, herein, these probes (organic ICG dye ICG) and AuNPs are encapsulated with cancer cells vesicles for metastasis theragnostic.

2. In vitro biocompatibility and optotheranostics performance

In vitro biocompatibility tests of BCMNVs, BCMNVs-ICG, and AuNPs@BCMNV-ICG NPs were performed with L929 cells and red blood cells (RBCs) at various concentrations (25–200 μg/mL). Upon NPs incubation, there was >90% of L929 viability and negligible hemolysis (below 3%) indicated the biocompatibility of these formulations due to the presence of the biomimetic components, such as surface biomarkers and lipid layer (Fig. 3a, b). Engineered nanovesicles were also capable of multiple cargo capacity beyond AuNPs and ICG dye. Prior to NIR light treatment, DOX (1100–1400 drug/NPs) was loaded into BCMNVs-ICG (48% cell death) and AuNPs@BCMNVs-ICG (55% cell death) showing a promising cell death (48% and 55%, respectively) of metastatic breast cancer cells (i.e., 4 T1 cells) due to their chemotherapeutics effect. Upon NIR treatment (10 min of exposure), DOX@AuNPs@BCMNVs-ICG (1.2×10^{11} nanoparticles/cm^3) induced about 90% of cell death, demonstrating synergistic effects of PTT heat treatment and chemotherapeutic release from the proposed platform (Fig. 3c). BCMNVs-ICG demonstrated about 82% of cell death, after NIR exposure, which was solely due to photosensitizing features of ICG dye. X-ray CT, NIRF, and PA

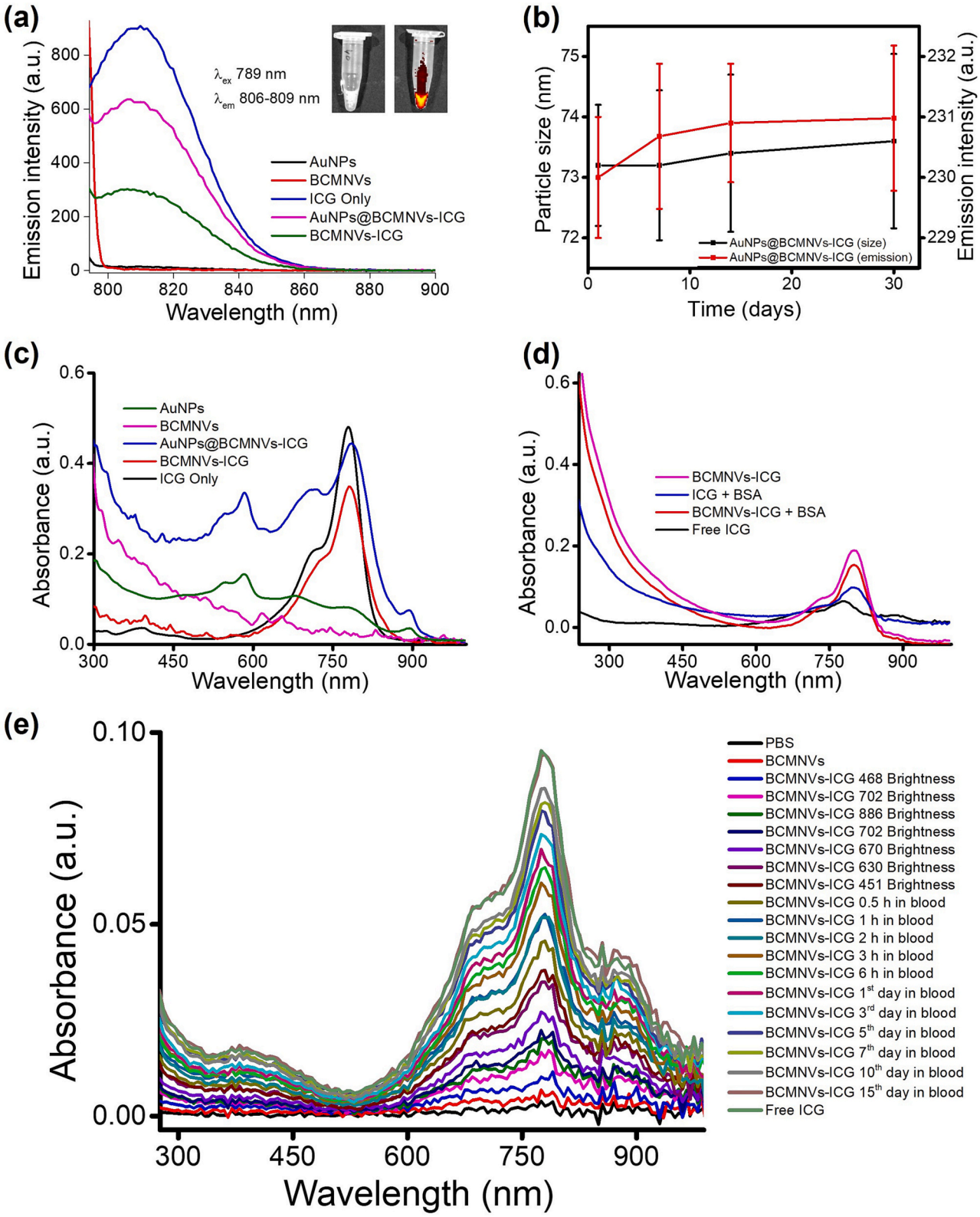

Fig. 2. (a) Photo luminance emission spectra of indocyanine green named as ICG dye encapsulated BCMNVs, AuNPs@BCMVs, free ICG dye, free BCMNVs and AuNPs (with and without AuNPs integration, 806–809 nm emission at 789 nm excitation), (b) particles and emission intensity measurements of ICG dye encapsulated AuNPs@BCMNVs at various time points (tested up to 30 days, all measurements were performed in triplicate, $n = 3$), (c) absorbance spectra of ICG dye encapsulated BCMNVs, AuNPs@BCMVs, free ICG dye, free BCMNVs and AuNPs, (d) absorbance spectra of BCMNVs and ICG dye encapsulated BCMNVs with and without BSA treatment and (e) absorbance spectra of ICG dye encapsulated BCMNVs for both brightness measurements and time dependent stability during blood circulation. (For interpretation of the references to color in this figure legend, the reader is referred to the web version of this article.)

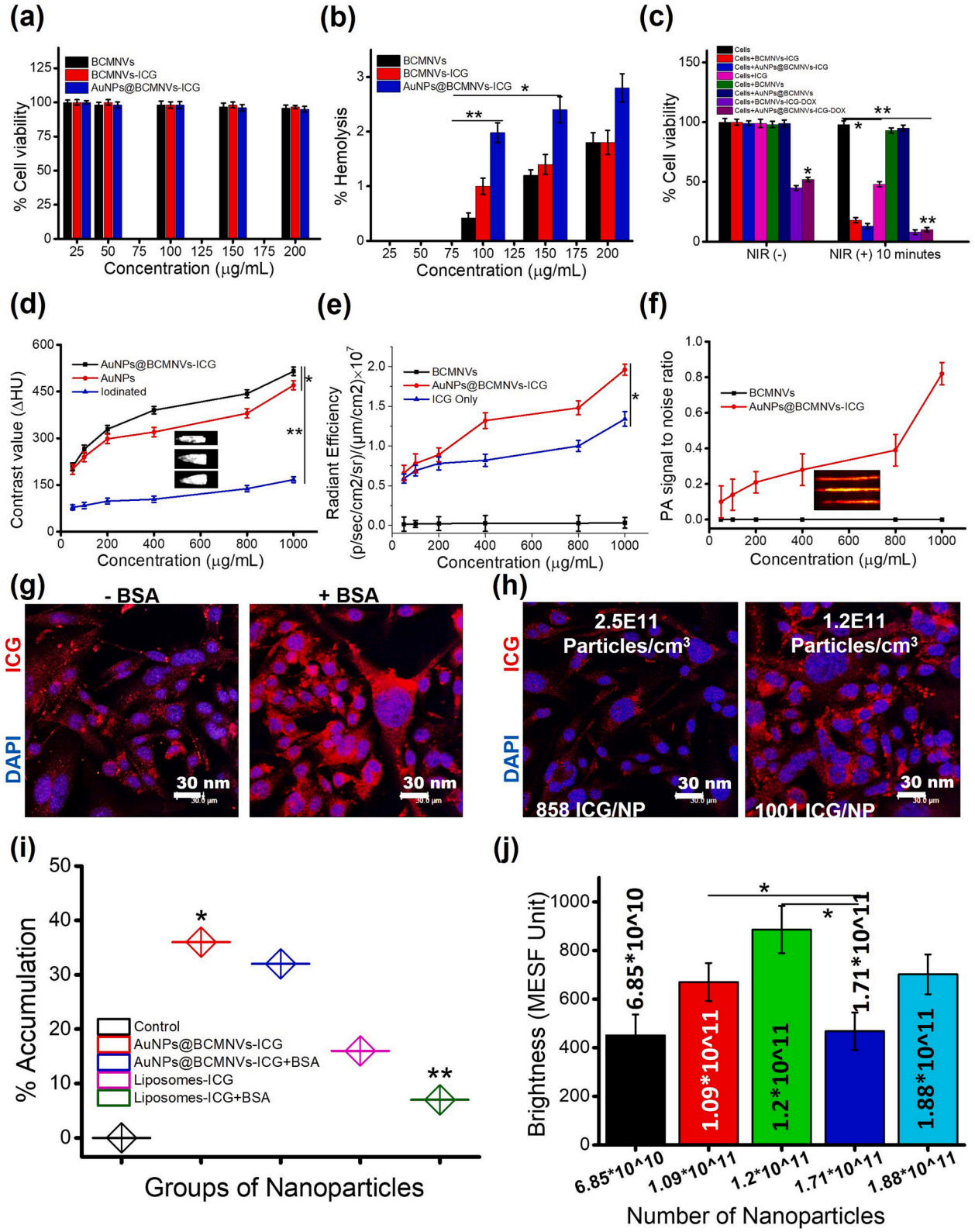

Fig. 3. Concentrations (50–1000 μg.mL^{-1}) dependent (a) % L929 viability and (b) % hemolysis of BCMNVs, BCMNVs-ICG and AuNPs@BCMNVs-ICG, (c) therapeutics efficacy of BCMNVs-ICG, BCMNVs-ICG-DOX, AuNPs@BCMNVs-ICG and DOX@AuNPs@BCMNVs-ICG before and after near infrared (NIR) light treatment, concentrations (50–1000 μg.mL^{-1}) dependent (d) radio density measurements, (e) red emissive contrast, (f) PA signal intensity, (g, h, i) cancer cell imaging and accumulation ability of AuNPs@BCMNVs-ICG before and after BSA treatment and (j) brightness counts in MESF units of AuNPs@BCMNVs-ICG with respect to average numbers of nanoparticle. *$p < 0.05$, **$p < 0.01$. All experiments were performed in triplicate ($n = 3$). (For interpretation of the references to color in this figure legend, the reader is referred to the web version of this article.)

imaging were also performed on AuNPs@BCMNVs-ICG NPs. In X-ray CT imaging, a significant rise in radiodensity (208 to 515 HU values) with respect to concentration (50–1000 μg/mL) was observed for AuNPs@BCMNVs-ICG (Fig. 3d). AuNPs@BCMNVs-ICG particles exhibited 3 times higher radio density than clinically used iodinated contrast agent (167 HU at 1000 μg/mL) due to the density and high atomic number of loaded AuNPs. In NIRF in vivo imaging system (IVIS) imaging, red emission (0.7×108–1.8×108 p/s/cm^2/sr) was observed from BCMNVs-ICG compared to free ICG dye at various concentrations (50–1000 μg/mL) following 745 nm excitation and 840 nm emission wavelengths (Fig. 3e and Fig. S8). At high concentrations, we observed a low red emission and brightness from free ICG dye that can be explained by quenching. On the other hand, BCMNVs-ICG NPs demonstrated uniform red fluorescent intensity as BCMNVs protect ICG dye from surrounding environment. Lastly, concentration dependent PA signal intensity and imaging of BCMNVs and AuNPs@BCMNVs-ICG were performed in a phantom using 2.72 MHz of L2 transducer, 832 nm of laser power, 5 mJ/cm^2 followed by 4 cm distance with a step size of 0.1 mm at different depths (30, 25, 20, 15, 10, 5 and 0 mm) (Fig. 3f and Fig. S9). Regular trend in signal intensity of PA was observed with respect to concentration (50–1000 μg/mL). Interestingly, a single system is capable of combine multimode imaging and therapeutics, hindering the multiple dose administration of nanotherapies that contain single imaging and/or therapeutic agents. Further, the proposed nanosystems do not require any additional surface functionalization to improve the biocompatibility and tumor targeting ability.

Next, these engineered biomimetic NPs were tested for targeted cancer cell imaging. To evaluate the cancer cell imaging, AuNPs@BCMNVs-ICG NPs were incubated with both murine and human metastatic breast cancer cells (Fig. 3g, h). Engineered nanoparticles demonstrated high uptake and broad distribution across locations within the cancer cell (cytoplasm and nucleus). To assess the potential hampered cellular uptake attributed to protein corona formation, we incubated engineered NPs with BSA prior to exposure to cancer cells. We observed no significant changes in cellular uptake and fluorescence from the cancer cell interior after BSA treatment (Fig. 3g). To qualitatively assess the amount of nanoparticles up taken per cell, different concentrations of nanoparticles (1.2×10^{11} and 2.5×10^{11} nanoparticles/cm^3) were incubated with 4 T1 and MCF-7 cells. Surprisingly, higher nanoparticle concentrations (2.5×10^{11} nanoparticles/cm^3) demonstrated poorer emission and possibly lower cellular uptake compared to lower concentrations (1.2×10^{11} nanoparticles/cm^3). This phenomenon can be due to high collision effect of freely dispersed NPs in aqueous medium, as shown in Fig. 3h. However, the clear mechanism is still unknown. Based on the distribution of fluorescent signal intensity from 4 T1 and MCF-7 cancer cells, accumulation efficacy of AuNPs@BCMNVs-ICG before and after BSA treatment was measured and compared with ICG dye tagged liposomal nanoparticles (4 T1 cells data shown in Fig. 3i and MCF-7 data shown in Fig. S11a). After NIR treatment, BCMNVs-ICG and AuNPs@BCMNVs-ICG demonstrated higher average red emission signal intensity and better accumulation within cancer cells than free conjugates and none NIR treatment exposure (Fig. S11b). The brightness (MESF units) of individual NPs with respect to number of dye/NPs was shown in Fig. 3j. Due to photothermally active ICG dye encapsulation, the engineered NPs demonstrated phototransduction response under NIR light exposure. In time dependent photo transduction experiments of BCMNVs-ICG and AuNPs@BCMNVs-ICG, the photo ablation temperatures (in the range of 47–53 °C) was recorded after 8 min of NIR light exposure (tested up to 10 min), which was further evaluated by phototransduction ON-OFF cycles (Fig. S11c, d). The engineered NPs were also tested for cancer therapeutics on breast cancer cells (MCF-7, non-metastatic). BCMNVs-ICG and AuNPs@BCMNVs-ICG showed 38% and 27% cell viability after 10 min of NIR light exposure due to their PDT therapeutics effect. Whereas DOX loaded BCMNVs-ICG and AuNPs@BCMNVs-ICG showed <20% cell viability after 10 min of NIR light exposure, which was due to the synergistic effect of produced PTT heat and released anticancer drug from the loaded NPs. Additionally, the PTT activity (>50 °C) of engineered theranostics system was ensured by measuring the reproducibility of temperature increase response over five heating cooling cycles upon NIR exposure (Fig. S11e). Overall, it was understood that specific numbers of ICG dye in BCMNVs indicated improved imaging and photothermal response. During in vivo photo transduction of AuNPs@BCMNVs-ICG (2.5×10^{11} nanoparticles/cm^3), the photo ablation temperatures (in the range of 47–53 °C) was recorded within 6 min of NIR light exposure indicated an improved therapeutics applicability, which was due to the high accumulation of injected NPs in solid tumor area (Fig. S11f). As mentioned above, the designed optotheranostics were capable of carrying multiple cargos viz., imaging agents (ICG dye and AuNPs) and therapeutics molecules (DOX). The release response of these cargo agents was evaluated in various pH (2–7.4) followed by spectroscopic measurements. In release kinetic patterns >80% release of loaded cargos viz., ICG, DOX and AuNPs within 12 h of incubation were calculated at lower pH (2–4) may be due to disintegration or dissembled optotheranostics platforms whereas at physiological condition optotheranostics nanoparticles demonstrated negligible release of loaded cargos (Fig. S12).

3. Multimode solid tumor imaging, biodistribution and tumor metastasis monitoring

Two different doses (2.5×10^{11} and 1.2×10^{11} nanoparticles/cm^3) of AuNPs@BCMNVs-ICG were intravenously administrated to 4 T1 tumor bearing female Balb/c mice. 6 h following injection, tumor was visible by the high brightness and uptake NPs levels, even at the lowest NPs concentrations (1.2×10^{11} nanoparticles/cm^3). Mirroring the surprising in vitro and in vivo uptake results, the highest dose administration (2.5×10^{11} nanoparticles/cm^3) showed lower tumor uptake and brightness than the low NPs dose. These observations were validated via three different imaging modalities such as NIRF, IVIS spectrum computed tomography, and PA imaging (Fig. 4a-h). In biodistribution measurements, high dose administration of AuNPs@BCMNVs-ICG NPs exhibited significant signal intensity (NIRF and radio density values) from the liver (0.9×10^7 p/s/cm^2/sr, ΔHU 190) and spleen (0.9×10^7 p/s/cm^2/sr, ΔHU 220) compared to low dose administration (liver; 0.6×10^7 p/s/cm^2/sr, ΔHU 80 and spleen; 0.38×10^7 p/s/cm^2/sr, ΔHU 94) (Fig. 4e,f). After low dose administration, a high contrast and signal intensities (2×10^7 p/s/cm^2/sr, ΔHU 480) were also observed from tumor areas. Furthermore, signal intensities in the heart (0.88×10^7 p/s/cm^2/sr) and lung (0.58×10^7 p/s/cm^2/sr) were seen in high dose administration compared to low dose NPs injection, which can be explained by NPs aggregation. Lastly, low concentrations of AuNPs@BCMNVs-ICG showed better contrast and signal intensities at the tumor site over time, up to 24 h (Fig. 4g). As a negative background control, the accumulation of injected NPs displayed much higher photoacoustic signal intensity from tumor area compared to the pre-injected tumor site (Fig. 4h).

4 T1 cancer cells for lung and liver metastasis caused by circulating tumor cells have been well studied and documented in the literature. However, longitudinal monitoring of lung and liver metastases sites at early stage was difficult to achieve so far. Herein, the 8 weeks old tumor bearing female mice were imaged for lung and liver metastasis observation using a single dose (1.2×10^{11} nanoparticles/cm^3) of AuNPs@BCMNVs-ICG NPs. These NPs accumulated in potentially metastatic areas of the lung and liver generated by deposition of circulating 4 T1 cancer cells. Whole body NIRF imaging and bioluminescence imaging at different times (1, 3, 7 and 15 days after the 10th day of primary tumor growth) revealed signal intensities from lung (1.2×10^7 to 2.5×10^7 p/s/cm^2/sr) and liver (1.7×10^7 to 2.8×10^7 p/s/cm^2/sr) metastases as well as the primary 4 T1 tumor in the mammary fat pad (2.2×10^7 to 3.2×10^7 p/s/cm^2/sr) (Fig. S13).

For biodistribution evaluation, single dose (1.2×10^{11} nanoparticles/cm^3) of AuNPs@BCMNVs-ICG NPs was injected to almost 7-

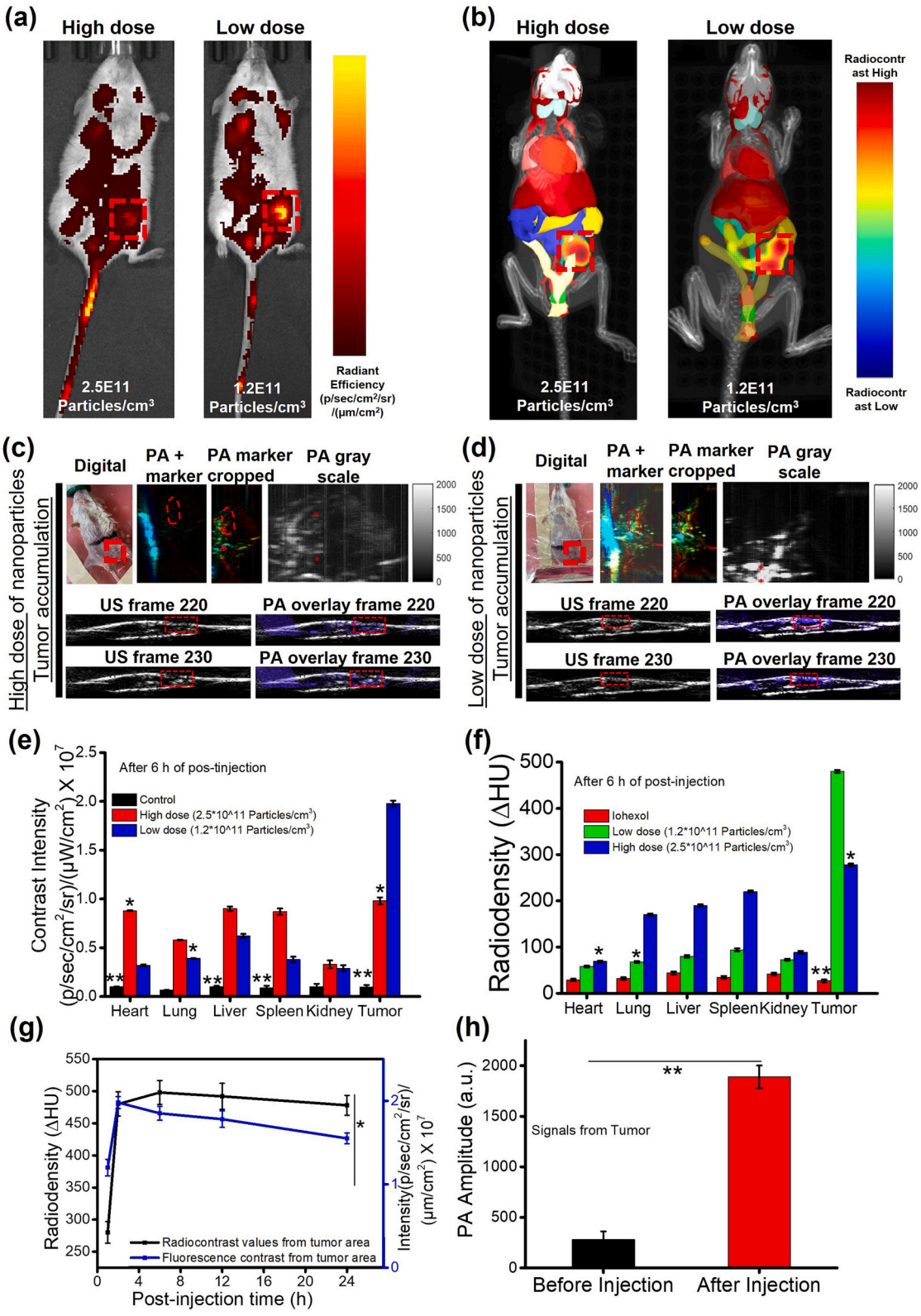

Fig. 4. Dose dependent multimode solid tumor imaging and bio-distribution analysis of intravenously (iv) injected AuNPs@BCMNVs-ICG (2.5×10^{11} and 1.2×10^{11} nanoparticles/cm^3). Whole body (a) near infrared fluorescence (NIRF) imaging, (b) in vivo imaging system (IVIS) Spectrum computed tomography (CT) and (c,d) photoacoustic (PA) imaging of targeted solid tumor imaging and bio distribution, (e) in vivo near infrared fluorescence (NIRF) imaging signal intensity profile and (f) radiodensity (RD) measurements from major organs and tumor area after injecting AuNPs@BCMNVs-ICG, (g) time dependent radio density (RD) and near infrared fluorescence (NIRF) signal intensity from tumor area of post-injected animals after low NPs dose injection and (h) photoacoustic (PA) signal intensity from tumor area after low NPs dose injection and compared to pre-injected tumor bearing animals. *$p < 0.05$, **$p < 0.01$. All measurements were performed in triplicate ($n = 3$).

week-old tumor bearing female mice. These post-injected mice were placed for whole body NIRF scans for emission intensity measurements and IVIS spectrum computed tomography scanning to measure radio density from major organs (heart, liver, spleen and kidney) and tumor at different time points of post-injection (0.5 h to 168 h) (Fig. 5a,b). The deep visualization of tumor site (25 pmol M^{-1} cm^{-1} from IVIS spectrum computed tomography and 3.1 × 10^7 p/s/cm^2/sr from NIRF after 168 h of post-injection) was ensured by measuring better signal intensities from these multimode imaging modalities. Further, signal intensity of injected AuNPs@BCMNVs-ICG from heart (17 pmol M^{-1} cm^{-1} and 1.9 × 10^7 p/s/cm^2/sr), liver (11 pmol M^{-1} cm^{-1} and 1.4 × 10^7 p/s/cm^2/sr) and spleen (6 pmol M^{-1} cm^{-1} and 1.2 × 10^7 p/s/cm^2/sr) was gradually decreased and increased in the tumor area (2 to 25 pmol M^{-1} cm^{-1} and 0.8 × 10^7 to 3.1 × 10^7 p/s/cm^2/sr) with respect to post-injection time (0.5 h to 168 h) indicating the specific biodistribution and tumor accumulation ability of the injected nanosystem (Fig. 5c,d). Interestingly, it was noted that low dose administration of AuNPs@BCMNVs-ICG (1.2 × 10^{11} nanoparticles/cm^3) exhibited maximum signal intensity from tumor area (Δ Hounsfield Units named as HU 512) after 24 h of post-injection which was further reduced with respect to post-injection time (48 h to 168 h, ΔHU 488 to ΔHU 310). Whereas it was insignificant in liver with respect to administration time (48 h to 168 h, ΔHU 53 to ΔHU 32) and similar pattern was observed from NIRF imaging bio-distribution (Fig. 5e, f). Apart from this, lung and liver metastasis caused by circulating 4 T1 cells were cross checked through histopathology examinations (Fig. 5g, h). PA imaging modality was applied to examine solid tumor location in female mice (Fig. S14, S15). Post-injection mice were imaged with L2 Transducer, 2.72 MHz, 832 nm laser and 4.6 mJ/cm^2 laser power where ultrasound was greyscale which was overlaid with PA signal in purple. The circulation half-life ($t_{1/2}$) of injected NPs was measured about 8 ± 1 h (Fig. 5i, see details in the supporting information). Blood circulation lifetime of intravenously injected AuNPs@BCMNVs-ICG was evaluated by estimating the gold by inductively coupled plasma-mass spectrometry.

4. Multimode therapeutics for image guided solid tumor growth inhibition

Synergistic (chemo-PTT-PDT) and single (chemo, PTT, and PDT) treatments of designed optotheranostics were performed in five groups of solid tumor-bearing female mice (Fig. 6). After 3 h of the intravenously NP injection (1.2 × 10^{11} nanoparticles/cm^3) into 4 T1 tumor-bearing female mice, several therapeutic treatments were administered and compared: (i) AuNPs@BCMNVs-ICG-DOX under NIR light irradiation (800 nm, 0.5 W power, and 10 min for light exposure) for evaluation of combined treatment efficacy (chemo-PTT-PDT), (ii) AuNPs@BCMNVs-ICG-DOX without NIR light treatment to study only delivered chemo efficacy, (iii) AuNPs@BCMNVs-ICG under NIR light irradiation for only PDT efficacy, (iv) BCMNVs-ICG under NIR light treatment was for PTT therapeutics of solid tumor ablation, and (v) a negative control, pre-injected mice condition named as 'no therapeutics'. On the 15th day of therapeutics course, image guided tumor ablation and growth inhibitions were assessed by measuring signal intensities from tumor area obtained by NIRF, IVIS spectrum computed tomography, and luciferase responsive bioluminescence imaging (Fig. 6 and Fig. S16). Among the five treatment conditions, the synergistic chemo-PTT-PDT therapy showed the highest tumor volume reduction (201 mm^3) and the highest signal intensity (5 pmol M^{-1} cm^{-1} and 0.6 × 10^7 p/s/cm^2/sr). Specifically, the efficacy of synergistic therapy was significantly enhanced beyond standalone chemo (22 pmol M^{-1} cm^{-1} and 2.6 × 10^7 p/s/cm^2/sr), PTT (9 pmol M^{-1} cm^{-1} and 0.9 × 10^7 p/s/cm^2/sr) and PDT (12 pmol M^{-1} cm^{-1} and 1.5 × 10^7 p/s/cm^2/sr) based on signal intensity (Fig. 6a, b and Fig. S16). About 0.5 g loss in body weight (~22.4 to ~21.9 g) was noticed after combined and standalone therapeutic treatments as compared to control (Fig. 6c). Substantial reduction in tumor volume (201 to 61 mm^3) and weight (0.61 to 0.15 g) were measured in the case of synergistic chemo-photothermal-photodynamic therapeutic under NIR light exposure as compared to pre-injected animals (no therapeutic) (Fig. 6d and Fig. S17). Single chemo, PDT, and PTT Showed successive tumor volumes (134, 72 and 88 mm^3) and tumor weight (0.42, 0.33 and 0.25 mg) reduction, respectively (Fig. 6d and Fig. S17). NIR light triggered synergistic chemo-PTT-PDT not only reduced the overall tumor growth but also improved the survival times of treated animals for 7 weeks on average (Fig. 6e).

5. Optotheranostics for image guided tumor metastasis monitoring and growth inhibition

4 T1 cells expressing mCherry [53] were orthotopically injected into female Balb/c mice to establish lung and liver metastasis. 10 days after injection, lung and liver metastases were imaged via whole body IVIS spectrum computed tomography, in vivo fluorescence, luciferase responsive bioluminance, and radiocontrast imaging using injected AuNPs@BCMNVs-ICG NPs (1.2 × 10^{11} NPs/cm^3) (Fig. 7). Histopathology examinations showed the development of small tumor nodules in lung and liver tissue, clearly showing metastatic lesions (Fig. S18). As before, different formulations of engineered optotheranostic NPs were injected to demonstrate the benefits of synergistic chemo-PTT-PDT treatment versus single (chemo, PTT, or PDT) treatments for lung and liver metastasis growth inhibition (Fig. 7). Significant growth inhibition in lung and liver metastasis was observed in the case of intravenously injected AuNPs@BCMNVs-ICG-DOX under NIR light irradiation (890 bioluminescence count, 1 × 10^7 p/s/cm^2/sr, ΔHU 135) in comparison with the untreated condition (7600 bioluminescence count, 2.8 × 10^7 p/s/cm^2/sr, ΔHU 480) (Fig. 7 and Fig. S19). X-ray computed tomographic images validated the significant reduction in tumor nodules from lung area after synergistic chemo-PTT-PDT therapeutic compared to control (Fig. 7 and Fig. S20). In PDT therapy, the presence of minor tumor nodules was examined through X-ray computed tomographic images, but they were significantly low compared to the no treatment control. This indicated a low efficacy of single therapy for metastasis growth inhibition (Fig. 7d). These observations were corroborated by recording mCherry signals from lung and liver under 570 nm of excitation and 640 nm emission wavelengths. As mentioned above, there were no detected mCherry signals from the lung after chemo-PTT-PDT therapy. Also, no detectable mCherry signals from the lung were observed from PDT treatment (Fig. 7d). Ex-vivo fluorescent images depicting ICG emission demonstrated an accumulation of injected AuNPs@BCMNVs-ICG-DOX NPs, which indicated the presence of lung metastasis (Fig. 7e). Lung and liver metastasis growth were studied by histopathology examination and body weight measurements (Fig. 7e and Fig. S20). Controlled body weight (21 to 21.4 g) was measured in all single therapeutics courses whereas control group (no therapy) showed regular enhancement in body weight increment (21.4 to 23.6 g). Interestingly, constant body weight (21 g) was measured during synergistic therapeutic course during 13 days of observation (Fig. S20). Lung metastasis inhibition was examined through X-ray computed tomography imaging followed by chemo, PTT, PDT therapy and synergistic chemo-PTT-PDT therapy (Fig. S21).

6. Outlook

The results presented in this work illustrate the importance of developing cancer cells derived biomimetic bright optotheranostics for metastasis monitoring and multimodal image-guided breast cancer therapy. As of now, liposomes, silica, gold, iron and polymeric-based systems have been studied for solid tumor imaging and therapeutics. These systems, however, are largely limited by natural physiological barriers preventing effective accumulation of synthetic nanocarriers in solid tumors.Moreover, specific biodistribution, selective tumor targeting, reproducibility and scalability, multi modal imaging and

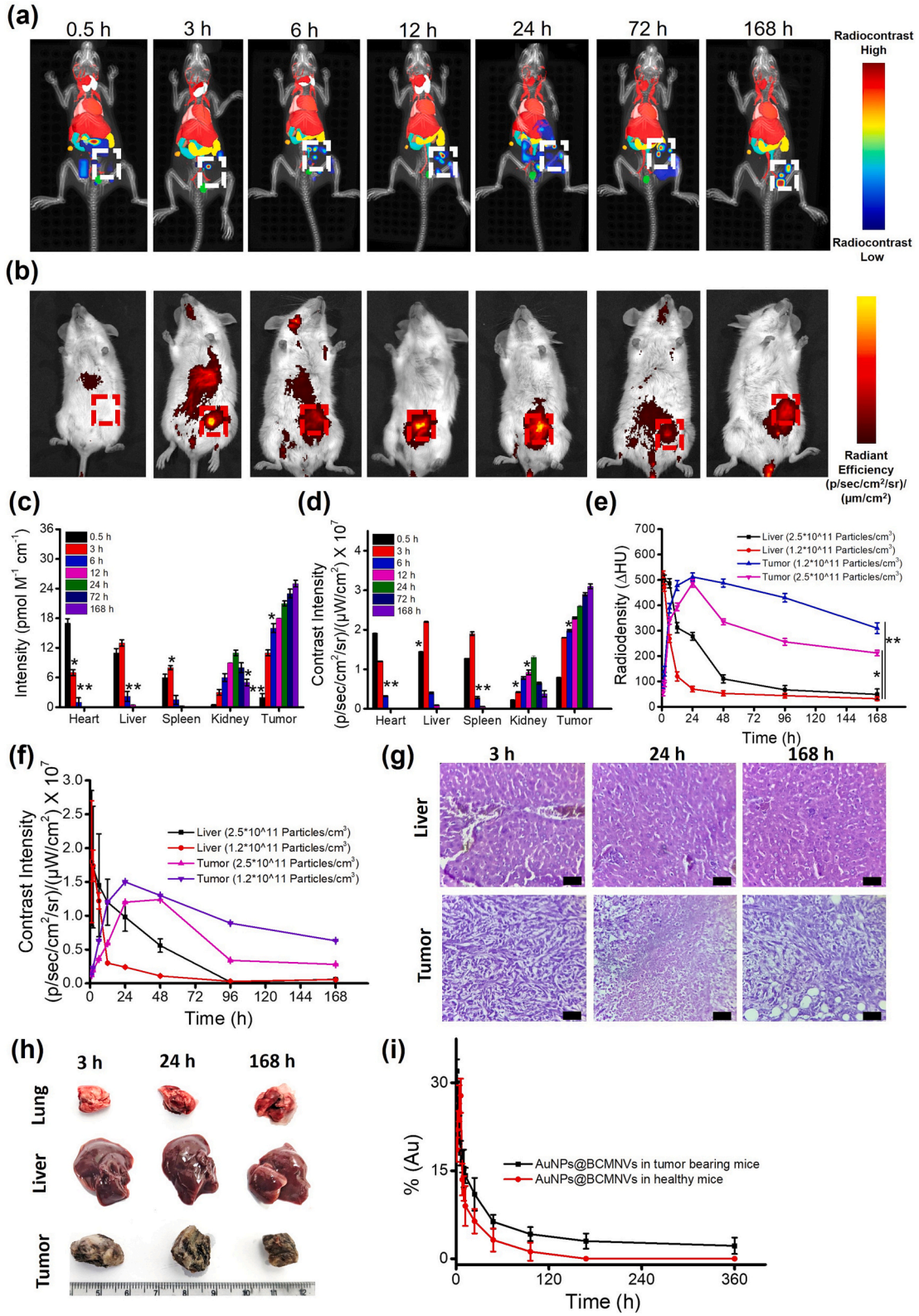

Fig. 5. Time dependent (0.5 h to 168 h) multimode solid tumor imaging and bio-distribution analysis of intravenously (iv) injected AuNPs@BCMNVs-ICG (1.2×10^{11} nanoparticles/cm^3). Whole body (a) in vivo imaging system (IVIS) spectrum computed tomography (CT) and (b) near infrared fluorescence (NIRF) imaging for targeted solid tumor imaging and bio distribution and (c,d) signal intensity measurements from heart, liver, spleen, kidney and tumor analyzed from in vivo near infrared fluorescence (NIRF) and in vivo imaging system (IVIS) spectrum computed tomography (CT), (e,f) time dependent (0.5 h to 168 h) signal intensity profile from liver and tumor after intravenously injected AuNPs@BCMNVs-ICG (2.5×10^{11} and 1.2×10^{11} nanoparticles/cm^3) measured from near infrared fluorescence (NIRF) and in vivo imaging system (IVIS) computed tomography (CT), (g) hematoxylin & eosin (H&E) of metastasized liver and tumor tissues obtained after 3 h, 24 h and 168 h, (h) digital photograph of metastasized lung, liver and tumor obtained after 3 h, 24 h and 168 h and (i) blood circulation lifetime of intravenously injected AuNPs@BCMNVs-ICG. *$p < 0.05$, **$p < 0.01$. All measurements were performed in triplicate ($n = 3$).

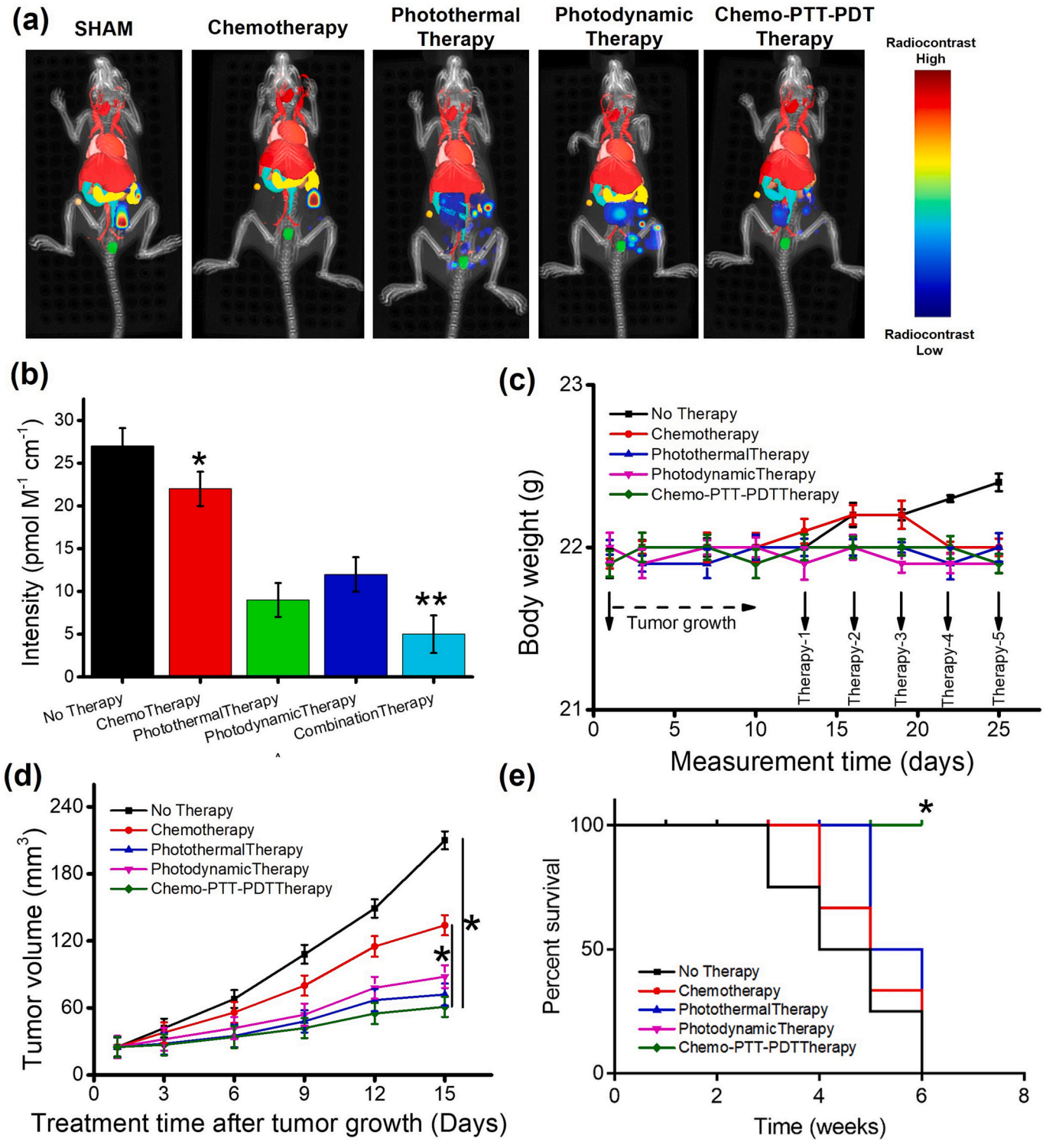

Fig. 6. Image guided solid tumor ablation measurements after various therapeutics courses of AuNPs@BCMNVs-ICG-DOX optotheranostics such as chemotherapy (chemo), photo thermal therapy (PTT), photodynamic therapy (PDT) and synergistic chemo-PTT-PDT therapeutics. (a) Whole body in vivo imaging system (IVIS) computed tomography (CT) imaging of treated mice, (b) signal intensity measurements for tumor ablation, (c) body weight measurements at various days of therapeutics course, (d) time dependent tumor volume measurements and (e) animal survival after therapeutics courses. Pre-injected mice were considered as control which was named as no Therapy. $*p < 0.05$, $**p < 0.01$. All measurements were performed in triplicate ($n = 3$).

therapeutics in combination at minimum dose administration are major concerns of any engineered nanotheranostics system. These aforementioned issues are limited due to lack of multiple cargo loading and their poor loading capacity, lack of inherent targeting agents, low colloidal stability, and low biocompatibility. In recent years, the development of biomimetic NPs such as cell membrane-coated nanoparticles and tumor/immune-cell derived nanovesicles have displayed the ability to overcome limitations of nonbiomimetic materials and avoid reticuloendothelial system clearance. Nano-delivery systems focused on biomimetic strategies can dramatically prolong circulation times, enhance tumor-

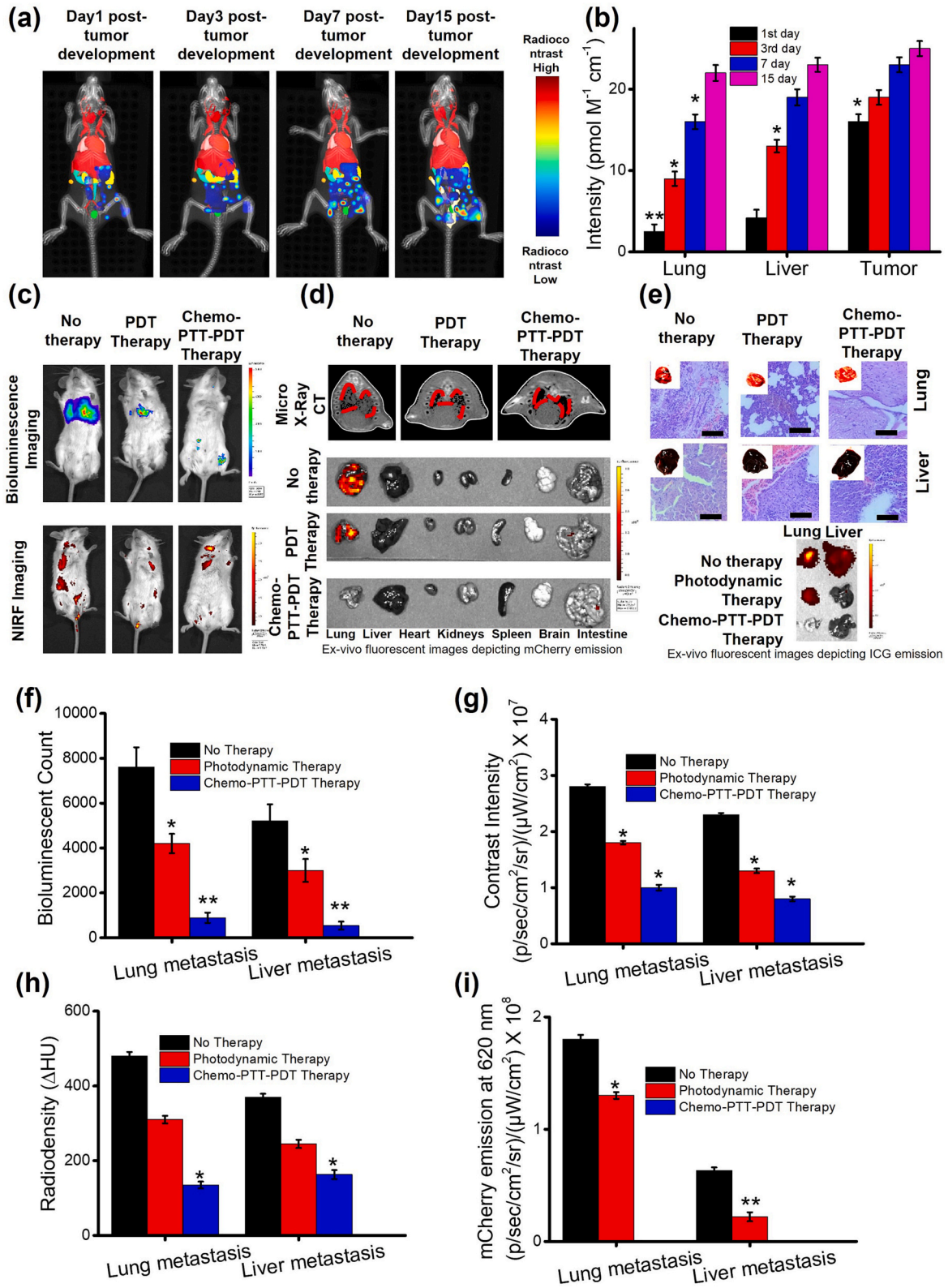

Fig. 7. Lung and liver tumor metastasis monitoring (a) whole body IVIS computed tomography imaging of optotheranostics injected mice and (b) signal intensity measurements from the site of metastasized lung, liver and mammary fat pad 4 T1 breast tumor at 1st, 3rd, 7th and 15th day. Image guided lung and liver tumor metastasis inhibition followed by photodynamic therapy (PDT) and synergistic chemo-PTT-PDT therapeutics using (c) bioluminescence and near infrared fluorescence (NIRF) imaging, (d) X-ray computed tomography (X-ray CT) and ex-vivo fluorescent images of lung, liver, heart, brain, kidneys, spleen and intestine representing mCherry emission, (e) hematoxylin & eosin (H&E) examinations and ex-vivo fluorescent images of lung and liver depicting ICG emission. Signal intensity measurements for lung and liver tumor metastasis inhibition using (f) bioluminescence, (g) near infrared fluorescence (NIRF) imaging, (h) X-ray computed tomography (X-ray CT) and (i) mCherry emission imaging analysis after photodynamic therapy (PDT) and synergistic therapeutics course. Pre-injected mice were named as no Therapy. $*p < 0.05$, $**p < 0.01$. All measurements were performed in triplicate ($n = 3$).

targeting abilities, and even potentially reveal early metastatic lesions. However, low scalability and poor reproducibility along with lack of multifunctionality are major concerns of such biomimetic hybrid systems. Until this work, however, the successful integration of multimodal imaging and therapeutics had yet to be achieved in a single biomimetic platform. By combining a photothermally active and red emissive organic dye, plasmonic AuNPs, and an anticancer drug within a single cell-derived nanovesicle platform (AuNPs@BCMNVs-ICG), we show the potential clinical benefits of utilizing multimodal imaging and combination therapy to diagnosis, monitor, and treat solid tumors in preclinical models.

In addition, breast cancer metastasis is another clinical challenge. The ability to monitor lung and liver metastasis in real-time and deliver targeted imaging and therapies could dramatically improve early-stage diagnosis and cancer treatment outcomes. The versatility of AuNPs@BCMNVs-ICG allows for the customization of diagnostics and therapeutic payloads, where the choice of imaging and therapeutics can be tailored to the specific characteristics of a patient's tumor. This combination approach optimizes triggered cargo/or drug delivery and minimize side effects without affecting surrounding healthy tissues. Additionally, the combination of chemo-PTT-PDT therapies has been tested for tumor reduction apart from single therapies, which significant enhance treatment efficacy at minimum dose requirement.

Detecting micro- and macro-metastases remains a significant challenge in cancer diagnosis and management. Most imaging modalities do not possess the resolution to detect metastatic lesions early, especially micro metastases. By the time metastases can be observed through imaging, the risk of cancer-associated mortality is already significant. As such, the potential ability of AuNPs@BCMNVs-ICG to monitor metastatic lesions in real-time with multiple imaging modalities provides a valuable tool for metastasis research. Researchers can explore ways to maximize the benefits of multiple imaging strategies once AuNPs@BCMNVs-ICG have accumulated at the target sites.

While the biocompatibility of AuNPs@BCMNVs-ICG was investigated in detail, ongoing research should continue to assess their long-term safety. Comprehensive toxicity studies in animal models can provide valuable insights into potential side effects and guide safety measures in clinical trials. In addition, the synergistic effect observed in the combined chemo-PTT-PDT therapy warrants further investigation. Future studies can focus on optimizing treatment protocols, dosages, and treatment schedules to maximize therapeutic outcomes while minimizing adverse effects. The continued research in cancer nanotheranostics and nanomedicine support the creation of even more sophisticated systems for targeted delivery of diagnostics and therapeutics.

In conclusion, the development of tumor-mimetic bright optotheranostics represents a significant advancement in cancer theranostics. The successful integration of imaging and therapeutic modalities within a biomimetic nanovesicle system holds great promise for improving cancer diagnosis, monitoring, and treatment.

7. Methods

7.1. Preparation of gold nanoparticles

The preparation of small gold nanoparticles was adopted from previously reported producers with some minor changes [37,54]. Briefly, a mixture of 100 μL of 0.05 M $HAuCl_4$, and 200 μL of 0.01 M sodium citrate was prepared in 10 mL of Milli-Q at 37 °C followed by high stirring. After complete mixing, 0.01 M $NaBH_4$ (100 μL of ice cold aqueous) as a reducing agent was added to the above mixture. Further, 2 mL volume from the prepared mixture was introduced to another mixture of 0.04 M CTAB, 5.0 mM $HAuCl_4$ and 0.1 M ascorbic acid. The whole mixing was done at 37 °C under vigorous stirring of the solution. Prepared gold nanoparticles were collected via centrifugation (10,000 rpm) and purified through dialysis overnight. These purified gold nanoparticles (AuNPs) were engineered with cancer cell derived cellular vesicles followed by mild incubation 37 °C. Further, surface modified gold nanoparticles were collected via centrifugation (10,000 rpm) and washed with PBS prior to further use.

7.2. Preparation of tumor-mimetic bright optotheranostics

Metastatic cell 4 T1 breast cancer cells were used to prepare tumor-mimetic membrane nanovesicles by hypotonic treatment through sonication. In brief, over confluent 4 T1 cells (5 × 10 [5]) were collected via centrifugation and washed with PBS (pH 7.4) followed by ice-cold Tris-Magnesium buffer washing using centrifugation (10,000 rpm). The washed cells were re-suspended in 10 mL of TM buffer for 10 min at 4 °C and then homogenized followed by mild sonication for 10 min. The obtained pellet was homogenized again and treated for a fridge thaw process (4–5 times) that break cells and then diluted with 10 mL of PBS and 5 mL of Tris-Magnesium buffer. The prepared suspension was centrifuged at 4 °C several times to collect the supernatant and pellet carefully. Further, the obtained colorless pellet was treated with 1× PBS and 20 mM Tris-Magnesium buffer for 1 h and then 0.1× PBS under slow stirring for 12 h. After complete stirring, the mixture was centrifuged and the pellet was further treated with hypotonic (a mixture of 20 mM Tris-Magnesium buffer, 0.2% HCL, and 0.1× PBS) suspension for overnight. Now the treated suspension was centrifuged at 10,000 rpm for 10 min and then collected supernatant and pellet separately, and the supernatant which contain small ghost cells was diluted with 10 mL PBS (pH 7.4). The diluted mixture was further treated for sonication (10 cycles) with 30% intensity and 5 s on/off the pulse and filtered under high pressure to achieve the nanosized cell membrane vesicles. To prepare bright optotheranostics, surface modified gold nanoparticles (5–6 nm, 0.05 mg/mL), ICG dye (0.01 mM) and cell membrane nanovesicles (1.08 mg/mL) were taken in a 1:1:5 volume ratio in the aqueous medium (PBS, pH 7.4) and then mixed at high stirring (1000 rpm). The prepared mixture was treated under sonication process (10 cycles) with 30% intensity and 5 s on/off the pulse in ice bath and filtered under high pressure. The obtained nanoparticles were dialyzed (12 kD mw cutoff) against 1000 mL DI water for 2 days at room temperature in dark conditions. Dialysate was changed in each 12 h. Further, brightness and photostability of designed nanoparticles were checked through spectroscopic measurements followed by mathematical calculations. For doxorubicin loading into nanoparticles, surface modified gold nanoparticles (5–6 nm, 0.05 mg/mL), ICG dye (0.01 mM), doxorubicin (0.01 mM) and cell membrane nanovesicles (1.08 mg/mL) were taken in a 1:1:1:5 volume ratio and then mixed properly prior to sonicate for 10 cycles at 30% intensity and 5 s on/off the pulse in ice bath. After sonication, the obtained suspension was filtered under high pressure and then dialyzed (12 kD mw cutoff) against 1000 mL DI water for 2 days at room temperature in dark conditions.

7.3. Photo-physicochemical performances

Different properties of designed nanoparticles such as ultra-brightness, photo stability, colloidal stability, aqueous dispersibility, and light to heat photo-transduction ability were measured from aqueous solution of nanoparticles (0.1 mg/mL) followed by microscopic and spectroscopic techniques. Colloidal stability and dispersibility of prepared nanoparticles in aqueous suspension were ensured by dynamic light scattering and turbidity measurements at different time points (1st day to 15th day). For these measurements, 50 μL aliquots of nanoparticle solution (0.1 mg/mL) were mixed to 200 μL of 10% *v*/v bovine serum albumin (BSA) diluted in phosphate-buffered saline (PBS) and incubated for 6 h at 37 °C to allow protein adsorption. To remove unbound serum, these incubated particles were washed three times of centrifugation (10,000 rpm for 30 min at 4 °C). After complete washing, the nanoparticles were resuspension in 1 mL of PBS (pH 7.4). Further, prepared aqueous solution of nanoparticles (0.1 mg/mL) and kept at 4 °C to measure the particles surface charge by zeta potential for 1st day to 30th

day. Fluorescence, brightness, and photostability of dye tagged nanoparticles were checked through photo luminance spectroscopic measurements at different time points (1st day to 15th day). Basic principle of fluorophores in flow cytometry was applied to measure the brightness of designed nanoparticles. A comparison between ICG dye tagged nanoparticles and ICG within the same spectral range indicated the brightness (see supporting information for more details). A single nanoparticle's brightness was calculated using the following equation:

$$\text{Brigthness} = \frac{(\text{Fluorescence intensity of a nanoparticle}/\text{Concentration})}{(\text{Fluorescence intensity of a dye}/\text{Concentration})}$$

Again, photostability was measured by considering both emission intensity and brightness at same concentrations (0.5/100 mg/mL) of free ICG and ICG tagged nanoparticles at different time points (1st day to 15th day). Light to heat response is also known as photo transduction performance of ICG, ICG tagged nanoparticles and gold nanoparticles encapsulated ICG tagged nanoparticles (0.1 mg/mL) was measured by using NIR laser (800 nm, 0.5 W power) for 10 min of exposure.

7.4. Multimode imaging

Triple imaging modality (X-ray Radiocontrast, Near Infrared Fluorescence and Photoacoustic Imaging) of ICG dye tagged nanoparticles (50–1000 μg/mL) were measured in an aqueous medium. 50 Voltage with 440 AI X-Ray filter was applied during X-ray scans. Total 720 projections were done during X-Ray contrast imaging and radio density values (Hounsfield Units, HU) were measured by using living image 4.1 and RadiAnt DICOM Viewer. A custom-made linear array transducer (Imasonic, Inc.) L2 with 2.72 MHz, 832 nm laser and 4.6 mJ/cm^2 laser power were used for US and PA imaging studies at in vitro and in vivo level and NIR fluorescence imaging were done by using in vivo imaging system (IVIS) at 745 nm of excitation wavelength with 840 nm of emission. Phosphate-buffered saline (PBS) was used as a control contrast for all imaging experiments. The radio density values in HU were measured by using RadiAnt DICOM Viewer software and following equation:

$$\text{Radio density (HU)} = \frac{(\text{HU value of suspended system} - \text{HU value of water})}{(\text{HU value of water} - \text{HU value of air})}$$

7.5. In vitro cell viability, hemocompatibility, cancer cell imaging and targeted multimode therapeutic

In vitro biocompatibility tests of engineered nanoparticles (only nanovesicles, ICG dye tagged nanovesicles, gold nanoparticles encapsulated ICG dye tagged nanovesicles, 25–200 μg/mL) were done with L929 healthy cells and red blood cells (RBCs). We followed our earlier reported methods to conduct these studies. For 24 h MTT assay, 2×10^5 density of L929 normal cells were seeded and incubated for 24 h with 5% CO_2 in Dulbecco's Modified Eagle's Medium (DMEM Gibco, Carlsbad, CA, USA). This culture medium was supplemented with 10% Fetal Bovine Serum and penicillin/streptomycin at 37.0 °C. After 24 h incubation, these cultured cells were treated with 50 μL total volume of nanoparticles from different concentrations (25–200 μg/mL). Further, these treated cells were washed with PBS after complete incubation and then 20 μL of MTT dye was added to check the % cell viability followed by formation of formazan crystals which were dissolved using 200 μL of DMSO. Cell viabilities were calculated by using $[\text{Abs}]_{\text{sample}}/[\text{Abs}]_{\text{control}} \times 100\%$; where $[\text{Abs}]_{\text{sample}}$ represents average absorption intensity of the sample containing the particles, and $[\text{Abs}]_{\text{control}}$ is the average absorption intensity of the control PBS. For hemocompatibility, healthy RBCs were used. In brief, collected healthy blood (1 mL) was diluted 10 times with PBS and further centrifuged (4000 rpm for 15 min) and washed thoroughly with PBS (pH 7.4). Finally, these collected RBCs were treated with various forms of nanoparticles (only nanovesicles, ICG dye tagged nanovesicles, gold nanoparticles encapsulated ICG dye tagged nanovesicles, 25–200 μg/mL) for 6 h (100 μL of RBCs and 900 μL of nanoparticles from each concentrations). After 6 h of treatment, mixtures were centrifuged at 4000 rpm for 15 min and absorption of released hemoglobin at 540 nm was measured by spectroscopic analysis, and % hemolysis was calculated using earlier reported equation mentioned below:

$$\text{Hemolysis (\%)} = \frac{(\text{Absorbance of sample} - \text{Absorbance of negative control})}{(\text{Absorbance of positive control} - \text{Absorbance of negative control})} \times 100$$

Targeted cancer cell imaging and % cell accumulation of nanoparticles were validated with metastatic 4 T1 and MCF-7 breast cancer cells. For these studies, breast cancer cells (2×10^5 cells/well) were cultured in DMEM culture media at 24 h incubation in 5% CO_2 at 37.0 °C. These cells were supplemented with 10% Fetal Bovine Serum and penicillin/streptomycin. After complete incubation, 2.5×10^{11} nanoparticles/cm^3 and 1.2×10^{11} nanoparticles/cm^3 of dye tagged nanoparticles (100 μL) were treated with 4 T1 and MCF-7 cancer cells. Herein, we have used both types of dye tagged nanoparticles (with and without serum treated nanoparticles). 4 h treated cells with nanoparticles were washed with PBS thoroughly to remove non-uptaken or non-accumulated nanoparticles. For confocal microscopy, treated cancer cells were fixed with 4% paraformaldehyde followed by cell nuclei staining with 4, 6-diamidino-2-phenylindole (DAPI). Further, cells were washed with PBS and mounted with the cover slip using a drop of 70% glycerol on glass slide and checked under fluorescence microscope. Further, % cell accumulation was considered based on intensities where untreated cells were considered as control group. Quantitative analysis of cellular uptake was performed on fluorescent images to explicitly calculate the degree of NPs uptake (**Fig. S10)**. From the images, to quantify ICG fluorescence, the Color Balance function in ImageJ/FIJI software was used to remove all blue channel signal. Once color adjusted, the subsequent image was converted to 8-bit color by scaling individual pixel intensity values to 0–255 for each red, green, and blue (RGB) channel and then individual cells were identified using segmentation processing. For these studies, background signal values were removed by thresholding and each pixel intensity within an individual cell was calculated by averaging individual RGB channel values. Fluorescent intensities at each pixel within cells were parsed into an array, binned by intensity (bin size of 1), and plotted as a histogram.

Next, in vitro targeted triple synergistic therapeutics (chemo-photothermal-photodynamic therapy) was tested on metastatic 4 T1 cancer cells and MCF-7 breast cancer cells using doxorubicin loaded gold nanoparticles encapsulated ICG dye tagged membrane nanovesicles named as AuNPs@BCMNVs-ICG-DOX. To examine the therapeutics performances of designed nanoparticles, metastatic 4 T1 and MCF-7 breast cancer cells were seeded at 2×10^5 cells/well in DMEM culture media and were cultured followed by 24 h incubation method. Further, these cultured cells were treated with 100 μL of AuNPs@BCMNVs-ICG-DOX nanoparticles (1.2×10^{11} nanoparticles/cm^3) under NIR light irradiation (800 nm, 0.5 W power, and 10 min for light exposure). Only gold nanoparticles encapsulated ICG dye tagged nanoparticles under

NIR light irradiation were used for combination photodynamic-photothermal therapeutics whereas doxorubicin loaded gold nanoparticles encapsulated ICG dye tagged membrane nanovesicles without NIR light irradiation was evaluated only for chemotherapy. Further, these treated cells were left for 24 h incubation and washed with PBS prior to use MTT dye (20 μL). In MTT formed formazan crystals were dissolved using DMSO, and % cell viabilities were calculated by considering untreated cells as control.

7.6. Cargo release (imaging and therapeutics probes) kinetics

Doxorubicin loaded ICG dye tagged gold nanoparticles encapsulated membrane nanovesicles (AuNPs@BCMNVs-ICG-DOX, 5 mL) were filled in a dialysis bag which was immersed into 100 mL of PBS with various pH values (2 to 7.4). At different time intervals, 3 mL solution was collected from dialysate and replaced with same volume of fresh PBS solution to maintain the constant volume. This was tested up to 48 h at room temperature. The amount of anticancer drug DOX (480 nm), gold nanoparticles (518–520 nm) and ICG dye (790–795 nm) in the release medium was checked by UV–Vis-NIR spectroscopic measurements.

7.7. Development of breast cancer mice model and tumor metastasis

Experimental protocols on Balb/c female mice were approved by the Institutional Animal Ethical Committee (IAEC) of the University at Buffalo, Sunny, New York, USA and the National Centre for Cell Science, Pune, India (NCCS, Pune). The IAEC allows us to conduct the in vivo experiments as per institute's guidelines. 2×10^5 4 T1 cells expressing mCherry were injected subcutaneously into the mammary fat pad of 6 weeks old female Balb/c mice and left for at least 10 days to grow the solid tumor. Tumor growth (in mm^3) was evaluated by $V = \pi/6\ (d1 \times d2)^{3/2}$, where d1 is the length and d2 is the width of the tumor. Tumor growth in individual groups was measured using caliper. Multimode imaging and therapeutics course began when significant budding of tumors (in few mm^3 volume) is noticed. For tumor metastasis towards lung and liver were measurements by two ways (1) examining multimode imaging of lung and liver site from 1st day of tumor growth (meant for 10th day of cell injection into the mammary fat pad) onwards to 15th day (meant for 35th day of cell injection into the mammary fat pad) and (2) 2×10^5 4 T1 cells expressing mCherry were injected intravenously and left for 10 days to see metastasis in lung and liver using NIRF, bioluminescence and X-ray CT imaging modalities.

7.8. In vivo tumor imaging, bio-distribution, and toxicity study of nanoparticles

Solid tumors were developed in female Balb/c mice by subcutaneous injection of 2×10^5 4 T1 breast cancer cells expressing mCherry in into the mammary fat pad. After the 10th day of significant tumor growth, two different doses (2.5×10^{11} nanoparticles/cm^3 and 1.2×10^{11} nanoparticles/cm^3) of ICG dye tagged gold nanoparticles encapsulated biomimetic nanoparticles were intravenously injected in tumor bearing mice. After 6 h post-injection, nanoparticles administrated animal models were placed for whole body scanning followed by triple imaging modalities (X-ray Radiocontrast CT, Near Infrared Fluorescence and Photoacoustic Imaging). Nanoparticles signals were measured from tumor area along with vital organs viz., heart, lung, liver, spleen, and kidneys. During these imaging modalities, 745 nm of excitation wavelength with 840 of emission has been applied for NIRF imaging, 50 kVp has been used for X-ray computed tomography and photoacoustic imaging were done under 2.72 MHz of L2 transducer, 832 nm of laser power, 5 mJ/cm^2 followed by 4 cm distance with a step size of 0.1 mm using 220 and 230 PA and US frame. Further, these scans were done at different time points of post-injection (0.5 h to 168 h) using same conditions. During triple imaging modality imaging scans of all mice ($n = 3$) were done in anesthetized condition. Various qualitative and quantitative analysis were done for understanding targeted tumor imaging and specific bio-distribution and compared with pre-injected mice as control group. In vivo toxicity of engineered optotheranostics agents was confirmed by conducting histopathological examinations (hematoxylin and eosin, H&E), body weight, blood biochemistry hemolysis analysis and animal survival measurements. A single dose of designed optotheranostics particles (1.2×10^{11} nanoparticles/cm^3) dispersed in PBS was (20 mg/kg body weight of 100 μL) was intravenously injected into female Balb/c mice (weight ~21–22 g) to evaluate the body weight and health measurements, blood circulation pharmacokinetic and histopathological examinations of vital organs. Moreover, spectroscopic analysis was done to measure the presence of gold in blood. In brief, 30–35 L blood was collected at various time points of post administration (1 h to 360 h) of nanoparticles from both healthy and tumor bearing mice. The collected blood samples were tested for ICP-MS and spectroscopic analysis followed by *aqua regia* treatment. Each day body weight measurement was done during tumor development and therapeutics course (tested up to 25 days, $n = 3$). Histopathology examinations (H&E staining) of vital organs at various time point (3 h, 24 h and 168 h) were conducted to investigate the tissue injuries.

7.9. Primary tumor growth and metastasis monitoring

For primary tumor growth measurements, solid tumors were developed by injecting 2×10^5 4 T1 breast cancer cells expressing mCherry into the mammary fat pad. After 10th day of significant tumor growth, 1.2×10^{11} nanoparticles/cm^3 of ICG dye tagged gold nanoparticles encapsulated biomimetic nanoparticles were intravenously injected in tumor bearing mice and placed for whole body scanning followed by X-ray Radiocontrast CT using micro-CT, Near Infrared Fluorescence and luciferase responsive bioluminescence imaging. Radio density, fluorescent and luciferase bioluminescence signals were measured from tumor area at different time points of post-injection (0.5 h to 168 h). Further, X-ray Radiocontrast CT, Near Infrared Fluorescence and luciferase responsive bioluminescence imaging were applied to notice tumor metastasis towards lung and liver followed by signal intensities from lung and liver site in case of (1) 1st day of tumor growth (meant for 10th day of cell injection into the mammary fat pad) onwards to 15th day (meant for 35th day of cell injection into the mammary fat pad). For developing lung metastasis, 4 T1 cells expressing mCherry were intravenously injected and left for 10 days of tumor growth. After 10 days of development, the lung metastasis in female mice was measured by whole body IVIS spectrum computed tomography, in vivo fluorescence, luciferase responsive bioluminescence and radio contrast imaging using post-injection of AuNPs@BCMNVs-ICG nanoparticles (1.2×10^{11} nanoparticles/cm^3). Additionally, mCherry signals from 4 T1 breast cancer cells were evaluated from the collected lungs after 10 days of post-injection. The collected lung tissues were tested for H&E. Photographs and histopathology of lung tissue clearly revealed lung metastasis. The development of small tumor nodules in the lung corroborated the successive lung metastasis in female mice. In vivo toxicity was examined by analyzing body weight of all the animal groups during the theranostics course (imaging and therapeutics). All imaging scans of mice (n = 3) were done in anesthetized condition. Both qualitative and quantitative analysis were done for understanding primary tumor growth and metastasis.

7.10. Multimodal image guided synergistic therapeutic of metastasis and solid tumors

In vivo targeted synergistic therapeutics (chemo-photothermal-photodynamic therapy) and standalone therapies (chemotherapy, photothermal therapy and photodynamic therapy) were tested on metastatic 4 T1 tumor and developed 4 T1 solid tumor. Therapeutics performances were done by intravenously injecting (1.2×10^{11} nanoparticles/cm^3) of doxorubicin loaded gold nanoparticles encapsulated

ICG dye tagged biomimetic nanoparticles and gold nanoparticles encapsulated ICG dye tagged biomimetic nanoparticles as opto-theranostics with and without NIR light irradiation (800 nm, 0.5 W power, and 10 min for light exposure). Therapeutics courses commenced after 3 h of post-injection of desired nanoparticles which were repeated for five therapeutic courses with 2 days' time intervals between each therapeutic course. Tumor growth inhibitions were measured by measuring signal intensities from tumor area followed by X-ray Radio-contrast CT, Near Infrared Fluorescence and luciferase responsive bioluminescence imaging on the 15th day of therapeutics course. On the other hand, lung and liver metastasis were treated by synergistic and standalone therapeutics such as chemo-photothermal-photodynamic therapy, chemotherapy, photothermal therapy and photodynamic therapy. These therapeutics courses were done by intravenously injecting engineered biomimetic nanoparticles (1.2×10^{11} nanoparticles/cm^3) viz., doxorubicin loaded gold nanoparticles encapsulated ICG dye tagged biomimetic nanoparticles with and without NIR light exposure with 2 days' time intervals between each therapeutic course. Reduction in lung and liver metastasis were corroborated with X-ray CT, Near Infrared Fluorescence and bioluminescence imaging. mCherry signals from lung and liver were recorded under 570 nm of excitation and 640 nm of emission. Both qualitative and quantitative analysis of tumor size, tumor volume, tumor weight was conducted during these studies.

7.11. Statistics

For statistical analysis, all experiments were performed in triplicate. All data were analyzed and plotted using OriginPro 8, GraphPad and sigma plot 10.0 software. Significant observations between different groups were calculated by *t*-test.

CRediT authorship contribution statement

Rajendra Prasad: Writing – review & editing, Writing – original draft, Visualization, Validation, Supervision, Project administration, Investigation, Funding acquisition, Formal analysis, Data curation, Conceptualization. **Berney Peng:** Writing – review & editing, Writing – original draft, Methodology, Investigation, Formal analysis. **Bárbara B. Mendes:** Writing – review & editing, Writing – original draft, Methodology, Investigation, Formal analysis, Data curation. **Hailey I. Kilian:** Writing – review & editing, Writing – original draft, Methodology, Investigation. **Mahadeo Gorain:** Writing – review & editing, Writing – original draft, Methodology, Investigation, Formal analysis. **Huijuan Zhang:** Writing – review & editing, Writing – original draft, Methodology, Investigation. **Gopal Chandra Kundu:** Writing – review & editing, Writing – original draft, Methodology, Investigation, Formal analysis. **Jun Xia:** Writing – review & editing, Writing – original draft, Validation, Supervision, Project administration, Funding acquisition, Formal analysis, Conceptualization. **Jonathan F. Lovell:** Writing – review & editing, Writing – original draft, Validation, Supervision, Project administration, Funding acquisition, Formal analysis, Conceptualization. **João Conde:** Writing – review & editing, Writing – original draft, Visualization, Validation, Supervision, Project administration, Methodology, Funding acquisition, Formal analysis, Data curation, Conceptualization.

Declaration of competing interest

J.C. is a co-founder and shareholder of TargTex S.A – Targeted Therapeutics for Glioblastoma Multiforme. J.C. is a member of the Global Burden Disease (GBD) consortium from Institute for Health Metrics and Evaluation (IHME), University of Washington (US). All the other authors declare no conflict of interest.

Data availability

Data will be made available on request.

Acknowledgements

R.P. would like to thank the Director and the School of Biochemical Engineering, Indian Institute of Technology (BHU), Varanasi for the support during preparation of this manuscript. R.P. also thanks the support of Tufts University, J.C. and B.B.M. acknowledge the European Research Council (Grant Agreement 848325). B.B.M., H.I.K., H.Z. and M.G. contributed equally to this project. We thank Dr. Gupta for critical reading of the manuscript and discussions on tumor imaging and therapeutic data. M.G. and G.C.K. thank support from NCCS, Pune and KIIT. H.I.K., H.Z., J.X. and J.F.L would like to thank the support from the University at Buffalo.

Appendix A. Supplementary data

Different data of designed opto-nanotheranostics have been mentioned in the supplementary information. Supporting data such as surface charge zeta potential, dispersion, absorption spectra, SAED, TEM images, EDAX, particle size DLS measurements, simulation information and data, in vitro IVIS, PA and X-Ray CT imaging, photo thermal experiments details, drug release kinetic pattern, in vitro biocompatibility and therapeutics, in vivo imaging (IVIS, X-Ray CT, PA, Bioluminescence) and related quantitative validations for tumor imaging and therapeutic studies, histopathology data were included. Supplementary data to this article can be found online at [https://doi.org/10.1016/j.jconrel.2024.01.056].

References

[1] L. Quetel, C. Meiller, J.B. Assié, Y. Blum, S. Imbeaud, F. Montagne, R. Tranchant, J. de Wolf, S. Caruso, M.C. Copin, V. Hofman, Genetic alterations of malignant pleural mesothelioma: association with tumor heterogeneity and overall survival, Mol. Oncol. 14 (6) (2020) 1207–1223.
[2] S. Ding, X. Chen, K. Shen, Single-cell RNA sequencing in breast cancer: understanding tumor heterogeneity and paving roads to individualized therapy, Cancer Commun. 40 (8) (2020) 329–344.
[3] A. Dent, P. Diamandis, Integrating computational pathology and proteomics to address tumor heterogeneity, J. Pathol. 257 (4) (2022) 445–453.
[4] C.M. Yamazaki, A. Yamaguchi, Y. Anami, W. Xiong, Y. Otani, J. Lee, N.T. Ueno, N. Zhang, Z. An, K. Tsuchikama, Antibody-drug conjugates with dual payloads for combating breast tumor heterogeneity and drug resistance, Nat. Commun. 12 (1) (2021) 3528.
[5] A. Marusyk, M. Janiszewska, K. Polyak, Intratumor heterogeneity: the rosetta stone of therapy resistance, Cancer Cell 37 (4) (2020) 471–484.
[6] D.T. Debela, S.G. Muzazu, K.D. Heraro, M.T. Ndalama, B.W. Mesele, D.C. Haile, S. K. Kitui, T. Manyazewal, New approaches and procedures for cancer treatment: current perspectives, SAGE Open Med. 9 (2021), 20503121211034366.
[7] W.D. Yu, G. Sun, J. Li, J. Xu, X. Wang, Mechanisms and therapeutic potentials of cancer immunotherapy in combination with radiotherapy and/or chemotherapy, Cancer Lett. 452 (2019) 66–70.
[8] S. Chupradit, G. Widjaja, B. Radhi Majeed, M. Kuznetsova, M.J. Ansari, W. Suksatan, A. Turki Jalil, B. Ghazi Esfahani, Recent advances in cold atmospheric plasma (CAP) for breast cancer therapy, Cell Biol. Int. 47 (2) (2023) 327–340.
[9] K.L. Zeng, A. Abugarib, H. Soliman, S. Myrehaug, Z.A. Husain, J. Detsky, M. Ruschin, A. Karotki, E.G. Atenafu, J. Larouche, M. Campbell, Dose-escalated 2-fraction spine stereotactic body radiation therapy: 28 Gy versus 24 Gy in 2 daily fractions, Int. J. Radiat. Oncol. Biol. Phys. 115 (3) (2023) 686–695.
[10] K.L. Zeng, A. Abugarib, H. Soliman, S. Myrehaug, Z.A. Husain, J. Detsky, M. Ruschin, A. Karotki, E.G. Atenafu, J. Larouche, M. Campbell, Dose-escalated 2-fraction spine stereotactic body radiation therapy: 28 Gy versus 24 Gy in 2 daily fractions, Int. J. Radiat. Oncol. Biol. Phys. 115 (3) (2023) 686–695.
[11] O. Saifi, W.G. Breen, S.C. Lester, W.G. Rule, B. Stish, A. Rosenthal, J. Munoz, S. M. Herchko, H.S. Murthy, Y. Lin, R. Bansal, Does bridging radiation therapy affect the pattern of failure after CAR T-cell therapy in non-Hodgkin lymphoma? Radiother. Oncol. 166 (2022) 171–179.
[12] S.P. Rowe, M.G. Pomper, Molecular imaging in oncology: current impact and future directions, CA Cancer J. Clin. 72 (4) (2022) 333–352.
[13] Y. Chen, S. Wang, F. Zhang, Near-infrared luminescence high-contrast in vivo biomedical imaging, Nat. Rev. Bioeng. 1 (1) (2023) 60–78.
[14] Z. Liu, F. Kiessling, J. Gätjens, Advanced nanomaterials in multimodal imaging: design, functionalization, and biomedical applications, J. Nanomater. 2010 (2010) 1–15.

[15] B.R. Smith, S.S. Gambhir, Nanomaterials for in vivo imaging, Chem. Rev. 117 (3) (2017) 901–986.
[16] R.D. Mehlenbacher, R. Kolbl, A. Lay, J.A. Dionne, Nanomaterials for in vivo imaging of mechanical forces and electrical fields, Nat. Rev. Mater. 3 (2) (2017) 1–17.
[17] S.M. Park, A. Aalipour, O. Vermesh, J.H. Yu, S.S. Gambhir, Towards clinically translatable in vivo nanodiagnostics, Nat. Rev. Mater. 2 (5) (2017) 1–20.
[18] P. Pei, Y. Chen, C. Sun, Y. Fan, Y. Yang, X. Liu, L. Lu, M. Zhao, H. Zhang, D. Zhao, X. Liu, X-ray-activated persistent luminescence nanomaterials for NIR-II imaging, Nat. Nanotechnol. 16 (9) (2021) 1011–1018.
[19] N. Kommineni, R. Chaudhari, J. Conde, S. Tamburaci, B. Cecen, P. Chandra, R. Prasad, Engineered Liposomes in Interventional Theranostics of Solid Tumors, ACS Biomaterials Science & Engineering, 2023.
[20] R. Prasad, N.K. Jain, J. Conde, R. Srivastava, Localized nanotheranostics: recent developments in cancer nanomedicine, Mater. Today Adv. 8 (2020) 100087.
[21] A.S. Thakor, S.S. Gambhir, Nanooncology: the future of cancer diagnosis and therapy, CA Cancer J. Clin. 63 (6) (2013) 395–418.
[22] A.S. Thakor, J.V. Jokerst, P. Ghanouni, J.L. Campbell, E. Mittra, S.S. Gambhir, Clinically approved nanoparticle imaging agents, J. Nucl. Med. 57 (12) (2016) 1833–1837.
[23] W. Poon, B.R. Kingston, B. Ouyang, W. Ngo, W.C. Chan, A framework for designing delivery systems, Nat. Nanotechnol. 15 (10) (2020) 819–829.
[24] W.C. Chan, Principles of nanoparticle delivery to solid tumors, BME Front. 4 (2023) 0016.
[25] W. Bian, Y. Wang, Z. Pan, N. Chen, X. Li, W.L. Wong, X. Liu, Y. He, K. Zhang, Y. J. Lu, Review of functionalized nanomaterials for photothermal therapy of cancers, ACS Appl. Nano Mater. 4 (11) (2021) 11353–11385.
[26] D. Nie, Z. Dai, J. Li, Y. Yang, Z. Xi, J. Wang, W. Zhang, K. Qian, S. Guo, C. Zhu, R. Wang, Cancer-cell-membrane-coated nanoparticles with a yolk–shell structure augment cancer chemotherapy, Nano Lett. 20 (2) (2019) 936–946.
[27] M.J. Ko, H. Hong, H. Choi, H. Kang, D.H. Kim, Multifunctional magnetic nanoparticles for dynamic imaging and therapy, Adv. NanoBiomed Res. 2 (11) (2022) 2200053.
[28] P.J. Gawne, M. Ferreira, M. Papaluca, J. Grimm, P. Decuzzi, New opportunities and old challenges in the clinical translation of nanotheranostics, Nat. Rev. Mater. (2023) 1–16.
[29] R. Zhang, F. Kiessling, T. Lammers, R.M. Pallares, Clinical translation of gold nanoparticles, Drug Deliv. Transl. Res. 13 (2) (2023) 378–385.
[30] T.I. Janjua, Y. Cao, C. Yu, A. Popat, Clinical translation of silica nanoparticles, Nat. Rev. Mater. 6 (12) (2021) 1072–1074.
[31] A.R. Rastinehad, H. Anastos, E. Wajswol, J.S. Winoker, J.P. Sfakianos, S. K. Doppalapudi, M.R. Carrick, C.J. Knauer, B. Taouli, S.C. Lewis, A.K. Tewari, Gold nanoshell-localized photothermal ablation of prostate tumors in a clinical pilot device study, Proc. Natl. Acad. Sci. 116 (37) (2019) 18590–18596.
[32] Y. Jiang, Z. Jiang, M. Wang, L. Ma, Current understandings and clinical translation of nanomedicines for breast cancer therapy, Adv. Drug Deliv. Rev. 180 (2022) 114034.
[33] P.P. Nayak, A. Narayanan, A.K. Badekila, S. Kini, Nanomedicine in cancer clinics: are we there yet? Curr. Pathobiol. Rep. 9 (2021) 43–55.
[34] H. Chen, W. Zhang, G. Zhu, J. Xie, X. Chen, Rethinking cancer nanotheranostics, Nat. Rev. Mater. 2 (2017) 17024.
[35] A. Dasgupta, I. Biancacci, F. Kiessling, T. Lammers, Imaging-assisted anticancer nanotherapy, Theranostics 10 (2020) 956–967.
[36] D. Ni, et al., Magnetic targeting of nanotheranostics enhances cerenkov radiation-induced photodynamic therapy, J. Am. Chem. Soc. 140 (2018) 14971–14979.
[37] R. Prasad, N.K. Jain, A.S. Yadav, D.S. Chauhan, J. Devrukhkar, M.K. Kumawat, S. Shinde, M. Gorain, A.S. Thakor, G.C. Kundu, J. Conde, Liposomal nanotheranostics for multimode targeted in vivo bioimaging and near-infrared light mediated cancer therapy, Communicat. Biol. 3 (1) (2020) 284.
[38] S. Sindhwani, A.M. Syed, J. Ngai, B.R. Kingston, L. Maiorino, J. Rothschild, P. MacMillan, Y. Zhang, N.U. Rajesh, T. Hoang, J.L. Wu, The entry of nanoparticles into solid tumours, Nat. Mater. 19 (5) (2020) 566–575.
[39] L.N. Nguyen, Z.P. Lin, S. Sindhwani, P. MacMillan, S.M. Mladjenovic, B. Stordy, W. Ngo, W.C. Chan, The exit of nanoparticles from solid tumours, Nat. Mater. (2023) 1–12.
[40] M. Izci, C. Maksoudian, B.B. Manshian, S.J. Soenen, The use of alternative strategies for enhanced nanoparticle delivery to solid tumors, Chem. Rev. 121 (3) (2021) 1746–1803.
[41] I. Khalin, D. Heimburger, N. Melnychuk, M. Collot, B. Groschup, F. Hellal, A. Reisch, N. Plesnila, A.S. Klymchenko, Ultrabright fluorescent polymeric nanoparticles with a stealth pluronic shell for live tracking in the mouse brain, ACS Nano 14 (8) (2020) 9755–9770.
[42] S.A.M. Peerzade, X. Qin, F.J. Laroche, S. Palantavida, M. Dokukin, B. Peng, H. Feng, I. Sokolov, Ultrabright fluorescent silica nanoparticles for in vivo targeting of xenografted human tumors and cancer cells in zebrafish, Nanoscale 11 (46) (2019) 22316–22327.
[43] B. Peng, M. Almeqdadi, F. Laroche, S. Palantavida, M. Dokukin, J. Roper, O. H. Yilmaz, H. Feng, I. Sokolov, Ultrabright fluorescent cellulose acetate nanoparticles for imaging tumors through systemic and topical applications, Mater. Today 23 (2019) 16–25.
[44] B. Ouyang, W. Poon, Y.N. Zhang, Z.P. Lin, B.R. Kingston, A.J. Tavares, Y. Zhang, J. Chen, M.S. Valic, A.M. Syed, P. MacMillan, The dose threshold for nanoparticle tumour delivery, Nat. Mater. 19 (12) (2020) 1362–1371.
[45] I. de Lázaro, D.J. Mooney, Obstacles and opportunities in a forward vision for cancer nanomedicine, Nat. Mater. 20 (11) (2021) 1469–1479.
[46] D. Wang, S. Wang, Z. Zhou, D. Bai, Q. Zhang, X. Ai, W. Gao, L. Zhang, White blood cell membrane-coated nanoparticles: recent development and medical applications, Adv. Healthc. Mater. 11 (7) (2022) 2101349.
[47] R.H. Fang, A.V. Kroll, W. Gao, L. Zhang, Cell membrane coating nanotechnology, Adv. Mater. 30 (23) (2018) 1706759.
[48] W. Liu, Y. Huang, Cell membrane-engineered nanoparticles for cancer therapy, J. Mater. Chem. B 10 (37) (2022) 7161–7172.
[49] Z. Zhao, C.B. Swartchick, J. Chan, Targeted contrast agents and activatable probes for photoacoustic imaging of cancer, Chem. Soc. Rev. 51 (3) (2022) 829–868.
[50] R. Wang, C. Song, A. Gao, Q. Liu, W. Guan, J. Mei, L. Ma, D. Cui, Antibody-conjugated liposomes loaded with indocyanine green for oral targeted photoacoustic imaging-guided sonodynamic therapy of helicobacter pylori infection, Acta Biomater. 143 (2022) 418–427.
[51] Y. Feng, B. Li, C. Jiang, F. Yang, Multifunctional gold nanorod composite for NIR imaging and photodynamic therapy treatment of tumor, Opt. Commun. 546 (2023) 129804.
[52] E. De Ravin, S. Venkatesh, S. Harmsen, E.J. Delikatny, M.A. Husson, J.Y. Lee, J. G. Newman, K. Rajasekaran, Indocyanine green fluorescence-guided surgery in head and neck cancer: a systematic review, Am. J. Otolaryngol. 43 (2022) 103570.
[53] A. Gilam, J. Conde, D. Weissglas-Volkov, N. Oliva, E. Friedman, N. Artzi, N. Shomron, Local microRNA delivery targets Palladin and prevents metastatic breast cancer, Nat. Commun. 7 (1) (2016) 12868.
[54] L.I. Silva, A. Perez-Gramatges, D.G. Larrude, J.M. Almeida, R.Q. Aucélio, A.R. da Silva, Gold nanoparticles produced using NaBH4 in absence and in the presence of one-tail or two-tail cationic surfactants: characteristics and optical responses induced by aminoglycosides, Colloids Surf. A Physicochem. Eng. Asp. 614 (2021) 126174.